

Mapping Thermal Conductivity at the Atomic Scale: A Step toward the Thermal Design of Materials

Chinonso Ugwumadu,* Aashish Gautam, Yoon Gyu Lee, and David A. Drabold*

We describe a spatial decomposition of the thermal conductivity, termed *site-projected thermal conductivity*, which quantifies the thermal conduction activity at each atomic site—a critical parameter for the thermal design of materials. The method is based on the Green–Kubo formula and the harmonic approximation and requires the force-constant and dynamical matrices, as well as a relaxed structural model. Throughout the study, it uses high quality models previously tested and compared to many experiments. It discusses the method and underlying approximations for amorphous silicon, carries the detailed analysis for amorphous silicon, and then examines an amorphous-crystal silicon interface and representative carbon materials. This study identifies the sites and local structures that reduce heat transport, and quantify these (estimate the spatial range) over which these “thermal defects” are effective. It identifies filamentary structures in the amorphous silicon network which impact heat transport and electronic structure (the Urbach edge) and electronic transport.

From the standpoint of materials design, the ability to predict atomistic or mesoscale transport is valuable. Perhaps the most obvious application of these methods is to thermoelectric materials,^[15] where control over heat flow relative to electrical conductivity is paramount.

One foundational theoretical framework stems from the pioneering work of Allen and Feldman (AF),^[1] and its extension by Feldman, Kluge, Allen, and Wooten (FKAW)^[2] in 1993. These studies formulated the thermal conductivity (TC) in the harmonic approximation for disordered, quantized lattices, applying it to amorphous silicon (a-Si). Using Wooten–Weaire–Winer-type^[16] structural models and the Stillinger–Weber potential for silicon,^[17] AF and FKAW established how vibrational modes contribute to thermal

transport in this homogeneously disordered system. Their work offered critical insights into the mode-resolved nature of heat conduction in amorphous materials, laying the foundation for decades of subsequent development.^[13,18–22]

From a materials design perspective, such a theory not only predicts global conductivity but can serve as a lens into local transport behavior. This is especially relevant for the identification of defective regions, interfacial bottlenecks, or thermally resistive motifs in heterogeneous materials. Spatially resolved thermal transport information could inform the targeted engineering of interfaces, heterostructures, and amorphous phases—guiding, for instance, the placement of dopants or the design of nanoscale thermal barriers to tune overall device performance.

Here, we extend the AF framework to extract *site-wise contributions* to thermal conductivity using a method we term the site-projected thermal conductivity (SPTC) approach.^[13] While the original AF formalism addresses the global question (“Given a structure and its force-constant matrix, what is the total thermal conductivity tensor?”), we demonstrate that this global quantity can be systematically decomposed to yield *local, atom-level estimates* of heat transport. In our initial report,^[13] we introduced the SPTC method and validated it on amorphous silicon (a-Si) by reproducing the benchmark results of AF and FKAW. We then applied the framework to more complex systems, including amorphous graphene, grain boundaries in crystalline silicon, and chemically disordered Si-Ge alloys, to investigate the impact of mass contrast and topological disorder on local heat transport behavior.

More generally, our approach allows for *spatial disentanglement* of transport behavior from a global Kubo-derived expression.^[23]


1. Introduction

The transport of heat is a key property of any solid. It is challenging to measure, difficult to compute, and currently the subject of lively debate surrounding new theories.^[1–14]

C. Ugwumadu
Quantum and Condensed Matter Physics (T-4) Group
Los Alamos National Laboratory
Los Alamos, NM 87545, USA
E-mail: cugwumadu@lanl.gov

A. Gautam, D. A. Drabold
Department of Physics & Astronomy
Nanoscale & Quantum Physics Institute
Ohio University
Athens, OH 45701, USA
E-mail: drabold@ohio.edu

Y. G. Lee
Department of Physics & Astronomy
Institute of Nuclear & Particle Physics
Ohio University
Athens, OH 45701, USA

 The ORCID identification number(s) for the author(s) of this article can be found under <https://doi.org/10.1002/pssb.202500316>.

© 2025 The Author(s). physica status solidi (b) basic solid state physics published by Wiley-VCH GmbH. This is an open access article under the terms of the Creative Commons Attribution-NonCommercial License, which permits use, distribution and reproduction in any medium, provided the original work is properly cited and is not used for commercial purposes.

DOI: 10.1002/pssb.202500316

The Kubo formula relates transport coefficients to autocorrelation functions that involve all atoms in the cell. Yet in disordered materials, different atomic regions contribute unequally to transport—a phenomenon hidden in the global sum. Inspired by prior attempts at “space-projected conductivity” in electronic transport,^[24,25] we express the thermal conductivity, κ , as a *double spatial sum* over atomic sites and then reduce it to a *site-specific quantity* by summing out one index.

$$\kappa = \sum_{x, x'} \Xi(x, x') \Rightarrow \zeta(x) = \sum_{x'} \Xi(x, x') \quad (1)$$

where the object Ξ is extracted from the work of AF, and x and x' index sites in the cell, and $\zeta(x)$ represents the local contribution to TC from atom site x . This construction is analogous to the “Mulliken population analysis” in quantum chemistry,^[26,27] where the electron density matrix and overlap matrix are used to assign partial charges to atoms in a molecule (following Szabo and Ostlund,^[26,27] if ρ_e is the single-particle density matrix and S the overlap matrix in a single-orbital, site-centered representation, then the total number of electrons is $N = \text{Tr}(\rho_e S) = \sum_{\mu, \nu} \rho_{e\mu\nu} S_{\nu\mu}$, and the charge associated with site μ is $Q_\mu = (\rho_e S)_{\mu\mu}$).

The purpose of this study is twofold. First, we provide a detailed account of the SPTC formulation, clarifying approximations and convergence behavior. Second, we explore how structural disorder correlates with local transport efficiency, with the aim of illuminating microscopic design principles for thermal control in complex materials.^[28] The study is organized as follows: Section 2 introduces the SPTC formalism, followed by its implementation in Section 3. Section 4 benchmarks the method using large a-Si models and the ML-GAP potential,^[29] reproducing AF and FKA results. Section 5 extends the analysis to Si interfaces, suboxides, and sp² carbon, revealing a link between thermal and electronic transport. Finally, Section 6 outlines open questions and potential future directions.

2. A Local Estimate of Thermal Conductivity

2.1. Harmonic Approximation

Heat transport in materials generally involves both electrons and phonons. In this article, we restrict our attention to the phonon contribution. By invoking the harmonic approximation (HA), phonons emerge as the heat carriers. The potential energy U is given as

$$U = \frac{1}{2} \sum_{\gamma, \gamma'} \sum_{i, j} \sum_{\alpha, \beta} \phi_{ij}^{\alpha\beta}(\gamma, \gamma') u_{i\gamma}^{\alpha} u_{j\gamma'}^{\beta} \quad (2a)$$

$$\phi_{ij}^{\alpha\beta}(\gamma, \gamma') = \frac{\partial^2 E}{\partial u_{i\gamma}^{\alpha} \partial u_{j\gamma'}^{\beta}} \quad (2b)$$

where $\phi_{ij}^{\alpha\beta}(\gamma, \gamma')$ is the force constant matrix (FCM) and γ and γ' represent cells in a periodic system. $u_{i\gamma}^{\alpha}$ is the α Cartesian component of the displacement vector for the i th atom in the γ th cell. Using periodicity, we can write $u_{i\gamma}^{\alpha\mathbf{k}}(t)$ where \mathbf{k} is a wave vector that may be chosen within the Brillouin zone

$$u_{i\gamma}^{\alpha\mathbf{k}}(t) = \frac{1}{\sqrt{m_i}} \sum_m e_{i\mathbf{k}}^{\alpha m} e^{i(\mathbf{k} \cdot \mathbf{R}_{i\gamma} - \omega_m t)} \quad (3)$$

Here, m_i is the mass of the i th atom and $e_{i\mathbf{k}}^{\alpha m}$ is the polarization of the m th vibrational mode (with a total $3 \times N$ modes, for the N number of atoms in the cell) of the i th atom along α direction. The classical equation of motion with this *ansatz* leads to the usual eigenvalue problem

$$(\omega_m^{\mathbf{k}})^2 e_{i\mathbf{k}}^{\alpha m} = \sum_{\beta j} D_{ij}^{\alpha\beta}(\mathbf{k}) e_{j\mathbf{k}}^{\beta m} \quad (4a)$$

$$D_{ij}^{\alpha\beta}(\mathbf{k}) = \sum_{\gamma} \frac{1}{\sqrt{m_i m_j}} \phi_{ij}^{\alpha\beta}(0, \gamma) e^{i\mathbf{k} \cdot (\mathbf{R}_{j\gamma} - \mathbf{R}_{i0})} \quad (4b)$$

where $D_{ij}^{\alpha\beta}(\mathbf{k})$ is the dynamical matrix (DM) and the lattice Fourier transform of the FCM, $\phi_{ij}^{\alpha\beta}(0, \gamma)$. $\mathbf{R}_{j\gamma}$ is the position of the j th atom in the γ th cell. The eigenvalues and eigenmodes of $D_{ij}^{\alpha\beta}(\mathbf{k})$ are the vibrational frequency of the m th mode $\omega_m^{\mathbf{k}}$ and the polarization $e_{i\mathbf{k}}^{\alpha m}$.

2.2. Site-Projected Thermal Conductivity

At the Γ point of the phonon Brillouin zone, the vibrational normal modes are real. For such a case, the AF expression for TC, represented as κ , takes the form

$$\begin{aligned} \kappa = \frac{\pi \hbar}{48 T V} \sum_{m, n \neq m} \left[-\frac{\partial \langle f_m \rangle}{\partial \omega_m} \right] \delta(\omega_m - \omega_n) \frac{(\omega_m + \omega_n)^2}{\omega_m \omega_n} \\ \sum_{\eta} \sum_{\alpha, \beta} \sum_{\gamma, x, x'} \frac{e_{x\gamma}^{\alpha m} e_{x'\gamma'}^{\beta n}}{\sqrt{m_x m_{x'}}} \phi_{xx'}^{\alpha\beta}(0, \gamma) (R_{\gamma}^{\eta} + R_{xx'}^{\eta}) \\ \sum_{\alpha', \beta'} \sum_{\gamma', a, b} e_{a\gamma'}^{\alpha' m} e_{b\gamma'}^{\beta' n} \frac{1}{\sqrt{m_a m_b}} \phi_{ab}^{\alpha'\beta'}(0, \gamma') (R_{\gamma'}^{\eta} + R_{ab}^{\eta}) \end{aligned} \quad (5)$$

where m and n are the indices of the classical normal modes, f_m is the equilibrium occupation of the m th mode, and ω_m and $e_{i0}^{\alpha m}$ are the vibrational frequency (ω_m^0) and the polarization ($e_{i0}^{\alpha m}$). R_{γ}^{η} is the η th component of \mathbf{R}_{γ} ; $R_{xx'}^{\eta}$ is the η th component of $\mathbf{R}_{xx'}$. The thermal conductivity in Equation 5 is taken as an average of the diagonal components of the conductivity tensor.

Next, we seek to extract local information about thermal conduction within the AF picture. The AF form for TC may be rearranged as a double sum over spatial points (labeled x). Carrying this out, with Equation 5, we find

$$\kappa = \sum_{x, x'} \Xi(x, x') \quad (6)$$

where

$$\Xi(x, x') = \frac{\pi \hbar^2}{48 k_B T^2 V} \frac{1}{\sqrt{m_{x'} m_x}} \sum_{\eta} \sum_{\gamma} (R_{\gamma}^{\eta} + R_{xx'}^{\eta}) \sum_{m, n \neq m} \delta(\omega_m - \omega_n) \frac{(\omega_m + \omega_n)^2}{\omega_m \omega_n} \left(\frac{e^{\frac{\hbar \omega_m}{k_B T}}}{\left(e^{\frac{\hbar \omega_m}{k_B T}} - 1 \right)^2} \right) \sum_{\alpha \beta} \phi_{x, x'}^{\alpha \beta}(0, \gamma) e_x^{\alpha m} e_{x'}^{\beta n} \sum_{\gamma' ab} \sum_{\alpha' \beta'} \frac{1}{\sqrt{m_a m_b}} \phi_{a, b}^{\alpha' \beta'}(0, \gamma') e_a^{\alpha' m} e_b^{\beta' n} (R_{\gamma'}^{\eta} + R_{ab}^{\eta}) \quad (7)$$

Ξ is a real-symmetric matrix with units of thermal conductivity. We decompose the total TC into contributions depending on atomic position x by a summation of $\Xi(x, x')$ over all positions x'

$$\zeta(x) = \sum_{x'} \Xi(x, x') \quad (8)$$

We call $\zeta(x)$ the site-projected thermal conductivity (SPTC), interpreted as the contribution of atom at site x in the cell to the total TC of the system, since

$$\kappa = \sum_x \zeta(x) \quad (9)$$

For anisotropic systems or off-diagonal terms the conductivity tensor $\kappa_{\alpha\beta}$ local contributions can be obtained similarly.

2.3. Spectral Properties of Ξ

To probe the microscopic structure of thermal transport in disordered systems, it is instructive to examine the transport matrix $\Xi(x, x')$. Analogous to the role of the density matrix in electronic structure theory—which reveals delocalization, bonding characteristics, and charge distribution—the eigenvalue decomposition of Ξ provides a natural mode basis for interpreting thermal conduction. In this basis, the eigenvalues λ_{μ} act as effective transmission amplitudes, while the corresponding eigenvectors $\eta_{\mu}(x)$ describe the spatial profile of each heat-carrying mode. This representation enables a form of “modal spectroscopy” of heat transport, offering direct diagnostics of localization, the presence of dominant conduction channels, and the extent of spatial delocalization of thermal excitations.

The eigenvalue problem for the (real-symmetric) matrix, Ξ with dimensions of thermal conductivity, reads:

$$\Xi \eta_{\mu} = \lambda_{\mu} \eta_{\mu} \quad (10)$$

Ξ is traceless, $\sum_{\mu} \lambda_{\mu} = 0$, so that the density of states of Ξ has both positive and negative support. The spectral version (in the Ξ diagonal representation) of the thermal conductivity is

$$\kappa = \sum_{\mu, x, x' (x \neq x')} \lambda_{\mu} \eta_{\mu}(x) \eta_{\mu}(x') \quad (11)$$

This implies that there is also a “mode-projected” conductivity

$$\kappa_{\mu} = \lambda_{\mu} \sum_{x, x' (x \neq x')} \eta_{\mu}(x) \eta_{\mu}(x') \quad (12)$$

In this representation, the spectral version of the SPTC becomes

$$\zeta(x) = \sum_{\mu} \lambda_{\mu} [\eta_{\mu}^2(x) + \sum_{x' \neq x} \eta_{\mu}(x) \eta_{\mu}(x')] \quad (13)$$

We pause for a moment to link this to the electronic transport. The analogous eigenvalue problem for the space-projected electronic conductivity is ([24])

$$\Gamma \chi_{\mu} = \Lambda_{\mu} \chi_{\mu} \quad (14)$$

Here, Γ is obtained from the Kubo–Greenwood formula,^[23,30] as Ξ is from the Green-Kubo formula^[23,31] and the work of AF. Γ always displays a huge null space, meaning that the great majority of Λ were concentrated near zero. Electronic conduction activity was compactly represented with a small number of (Λ, χ) with $\Lambda \neq 0$.

For both the electronic and thermal cases, the eigenvectors for Γ and Ξ may be interpreted as a “modes of conduction” for electrons and heat, respectively. These seem to be akin to the “transmission eigenchannels” of electron transport,^[32] the conjugate eigenvalues being a transmittance for the particular mode.^[33,34] We discuss the individual contributions of the κ_{μ} for the case of a-Si below.

Also, in analogy with electronic structure theory, we can interpret Ξ as a “thermal density matrix,” ρ , since in the spectral language of Ξ

$$\Xi(x, x') = \sum_{\mu} \lambda_{\mu} \eta_{\mu}(x) \eta_{\mu}(x') = \rho(x, x') \quad (15)$$

from which we can also write

$$\kappa = \sum_{x, x'} \rho(x, x') = \sum_{x, x'} \Xi(x, x') \quad (16)$$

As an aside, we note that the decay of this “thermal density matrix” is governed by the decay of the FCM (see Appendix A).

2.4. Cell Size, Periodicity, and Anharmonicity Considerations

2.4.1. Supercell Size

A supercell appropriate for our approach must be large enough to prevent spurious interactions between an atom and its periodic images, a range determined by $\Xi(x, x')$. This requirement is related to requiring that the dominant phonon mean free paths are significantly shorter than the cell dimensions. FKA^W estimated a phonon mean free path as $l \approx 3D/\nu$, where D is the diffusivity and ν is the longitudinal sound velocity.^[2] For a-Si, they find $l \approx 8 \text{ \AA}$, significantly smaller than the cells we selected for a-Si. Additionally, for all systems examined here, the spatial convergence of $\zeta(x)$ is rapid, owing to the short-ranged nature of the FCM. We further analyze this decay behavior for a-Si in Section 4.2.

2.4.2. Periodicity

We employ Γ -point-only sampling under the assumption that the simulation supercells are sufficiently large. Also, using the Brillouin zone associated with the periodicity of the supercell leads to spurious (divergent) results for κ ^[35]. Thus, for both practical and theoretical reasons, we stick to Γ . In amorphous materials like a-Si, the absence of translational symmetry precludes the use of plane-wave phonons. Thermal transport is governed mostly by diffusons—nonpropagating, extended modes—while high-frequency vibrations are typically localized (or quasi-localized).^[36,37] This contrasts with crystalline solids, where harmonic thermal conductivity diverges independently of unit cell size.^[12,38]

2.4.3. Anharmonicity

We invoke the harmonic approximation as the natural and obvious first estimate for the lattice dynamics. The regularizing role of anharmonicity—especially in preventing the divergence of thermal conductivity—has been emphasized by Fiorentino et al.^[12] Future extensions of our framework could incorporate anharmonic effects via the Quasi-Harmonic Approximation,^[39] enabling more realistic modeling of temperature-dependent transport phenomena.

3. Computational Implementation

The SPTC framework is implemented in the C++ programming language using a collection of source files, hereafter referred to as *modules*. These modules adopt a procedural programming approach and are organized into four key stages, each responsible for a distinct part of the thermal transport pipeline. Parallelization is achieved using OpenMP directives,^[40] enabling efficient scaling for large systems with thousands of atoms and dense spectral sampling. The code is optimized for high-performance computation, with binary output files used extensively for storage and subsequent visualization or post-processing.

3.1. Post-Processing of Interatomic Force Constants

The module `DynMat_process.cpp` converts the real-space DM—typically obtained from first-principles calculations using the Vienna *Ab initio* Simulation Package (VASP)^[41] or from classical simulations using the Large-scale Atomic/Molecular Massively Parallel Simulator (LAMMPS)^[42]—into properly mass-weighted harmonic force constants suitable for lattice dynamics and thermal transport analysis.

The required inputs include atomic species, Cartesian coordinates, atomic masses, system dimensions, and the DM formatted in Cartesian coordinates. The DM is assumed to be a $3N \times 3N$ symmetric matrix representing interatomic force constants for a system of N atoms. These elements are parsed and stored in a 4D array: $[i][j][\alpha][\beta]$, where i and j are index atoms, and $\alpha, \beta = 0, 1, 2$ represent Cartesian directions. Symmetrization is enforced via

$$\phi_{ij}^{\alpha\beta} \rightarrow \frac{1}{2} (\phi_{ij}^{\alpha\beta} + \phi_{ji}^{\beta\alpha}) \quad (17)$$

ensuring physical reciprocity of interatomic interactions. The matrix is then mass-weighted according to

$$\phi_{ij}^{\alpha\beta} \rightarrow \phi_{ij}^{\alpha\beta} \cdot \sqrt{m_i m_j} \quad (18)$$

where m_i and m_j are the atomic masses of atoms i and j , respectively.

3.2. Harmonic Approximation and Phonon Mode Extraction

The module `HARMONIC_APPROXIMATION.CPP` performs phonon mode analysis by diagonalizing the mass-weighted FCM in Equation 2b. Input data include structural geometry, the harmonic force constants, and the target \mathbf{k} -point (typically Γ). The force constants are remapped into a 7D array: $[i][j][\alpha][\beta][dx][dy][dz]$, where dx, dy , and dz define the lattice translation vectors mapping atom j to periodic images with respect to atom i . This array stores the second derivatives of the total energy with respect to atomic displacements as discussed in Equation 2a.

From these, the DM diagonalization is performed with LAPACK's `zheevd` routine,^[43] yielding eigenvectors and eigenvalues. Outputs include the phonon frequencies (THz), mode-resolved eigenvectors, and corresponding eigenvalues. Atom-resolved eigenmodes are also exported for visualization and projection tasks.

3.3. Computing the Heat Current

The `SPTC_PREPROCESSING.CPP` module constructs the velocity-like coupling tensors required to evaluate site-projected thermal conductivity within the AF framework. It bridges the harmonic mode analysis and the final SPTC computation by producing the mode-resolved couplings $S_{ij}^{\alpha}(m, n)$ that quantify energy transfer between vibrational modes. We note that $S_{ij}^{\alpha}(m, n)$ is more commonly known as the heat current operator.^[37,44]

The module first reads all necessary data: mass-weighted force constants, phonon eigenvectors and frequencies, atomic positions, atomic masses, and system dimensions. It then constructs neighbor lists using a cutoff radius and computes the minimum image convention vectors ΔR_{ij}^{α} between all atomic pairs.

For each phonon mode pair (m, n) , and for each atom pair (i, j) , the heat current S is computed as^[13]

$$S_{ij}^{\alpha}(m, n) = \sum_{\mu\nu} \frac{e_i^{\mu m} e_j^{\nu n} \phi_{ij}^{\mu\nu}}{\sqrt{m_i m_j}} \Delta R_{ij}^{\alpha} \quad (19)$$

where $e_i^{\mu m}$ is the μ component of the eigenvector for atom i in mode m and $\phi_{ij}^{\mu\nu}$ is the mass-weighted force constant tensor. The outputs include the squared magnitude S_{ij}^2 and Cartesian components S_{ij}^x, S_{ij}^y , and S_{ij}^z , stored in binary files for efficient access in the final SPTC calculation. A pseudo-code for computing $S_{ij}^{\alpha}(m, n)$, including its mode and direction-resolved structure, is detailed in **Algorithm 1**.

Algorithm 1. Heat Current Tensor Construction (SPTC_PREPROCESSING.CPP).

Input: $\phi_{ij}^{\mu\nu}$, e_i^{nm} , $\{\omega_m\}$, m_i , and system coordinates
Output: $S_{ij}^{\alpha}(m, n)$ and $|S_{ij}(m, n)|^2$
 Read input data;
 Construct neighbor-list using cutoff radius;
 Compute minimum image vectors ΔR_{ij}^{α} for each site pair (i, j) ;
foreach atom pair (i, j) **do**
 foreach mode pair (m, n) **do**
 Initialize $S_{ij}^{\alpha}(m, n) \leftarrow 0$;
 Compute $S_{ij}^{\alpha}(m, n)$ using Equation 19;
 Compute $|S_{ij}(m, n)|^2$ with $S_{ij}^{\alpha}(m, n)$;
 Store: neighbor list, ΔR_{ij}^{α} , $|S_{ij}|^2$, S_{ij}^x , S_{ij}^y , and S_{ij}^z ;

3.4. Computing SPTC

The final module, SPTC_CALCULATION.CPP, constructs the site-projected thermal conductivity tensor based on the precomputed heat current tensor and phonon mode data. Using the inputs from Section 3.2 and 3.3, the code assembles the thermal transport matrix $\Xi(i, j)$, as defined in Equation 7, for a user-specified list of frequencies.

The core of the computation is the construction of the transport (Ξ) matrix following Equation 7 with a defined width for the Lorentzian broadened delta function. The script then loops over a list of user-defined frequencies and accumulates thermal coupling strengths from all relevant mode pairs. Each entry in Ξ corresponds to energy transfer between two atomic sites mediated by vibrational coupling and can be projected into Cartesian coordinates α , as $\Xi^{\alpha}(i, j)$. Once Ξ is constructed, the thermal activity is projected onto atomic sites according to Equation 8 and summed across all sites to yield the total conductivity, as in Equation 9.

The Ξ matrix is optionally diagonalized to obtain its spectral structure and determine the modes of thermal conduction. The matrix is diagonalized using dsyevd.^[43] The eigenvalues and eigenvectors are stored for further modal and localization

Algorithm 2. Site-Projected Thermal Conductivity Calculation (SPTC_CALCULATION.CPP).

Input: $S_{ij}^{\alpha}(m, n)$, $\{\omega_m\}$, neighbor-list, ΔR_{ij}^{α} , and broadening parameter ϵ ,
Output: $\Xi^{\alpha}(i, j)$, $\zeta(i)$, and spectral data
 Read input data;
 Initialize $\Xi^{\alpha}(i, j) \leftarrow 0$ for all i, j , and α ;
foreach atom pair (i, j) **do**
 foreach mode pair (m, n) **do**
 Compute Lorentzian weight (see Section 4.4):

$$\delta(\omega_m - \omega_n) = \frac{\epsilon}{\pi((\omega_m - \omega_n)^2 + \epsilon^2)}$$

foreach polarization directions (μ, ν) **do**
 Accumulate contribution to $\Xi^{\alpha}(i, j)$ with $S_{ij}^{\alpha}(m, n)$ using Equation 7;
foreach atom i **do**
 Compute site conductivity

$$\zeta(i) = \sum_{j, \alpha} \Xi^{\alpha}(i, j) \quad (\text{Equation 8})$$

 Compute total conductivity

$$\kappa = \sum_i \zeta(i) \quad (\text{Equation 9})$$

 Optionally diagonalize $\Xi^{\alpha}(i, j)$ using dsyevd to get eigenvalues and eigenvectors;
 Store: $\Xi^{\alpha}(i, j)$, $\zeta(i)$, κ , and eigen-spectra;

analysis. Outputs include frequency-resolved site-level conductivity, the full transport matrix, and spectral decompositions. A pseudo-code for constructing the transport matrix, $\Xi^{\alpha}(i, j)$, and the corresponding site-resolved conductivity, $\zeta(i)$, is outlined in Algorithm 2.

3.5. Interatomic Interactions

All simulations utilized highly accurate Gaussian Approximation Potentials (GAP) for silicon,^[29] silicon-oxide,^[45] and carbon.^[46] Structural relaxations were performed using LAMMPS, with an energy convergence criterion of $\Delta E = 10 \times 10^{-6}$ eV. The DM was constructed via finite displacements of 0.05 Å along each Cartesian direction. The SPTC method is easily adapted to *ab initio* interactions. We have demonstrated compatibility with VASP, although the computation of force constants in this case is significantly more demanding.

4. Amorphous Silicon

In this section, we apply the method to a-Si both to test and understand the method and also because it is a classic disordered system, explored in a vast experimental and theoretical literature.^[47,48]

We employ structurally credible a-Si models generated with the Wooten–Winer–Weaire (WWW)^[16] approach, as implemented by Djordjević, Thorpe, and Wooten,^[49] and studied in Ref. [50] Systems containing 64, 216, 512, and 4096 atoms were analyzed to test our method against previous studies, track size effects and explore new features of TC in a-Si. The models were well relaxed using the same “annealing schedule,” and all atoms were four-coordinated.

4.1. SPTC Representation of Locon, Propagon, and Diffuson Regions of the Vibrational Spectrum

AF classify vibrational modes in disordered solids into three categories: *propagons*, *diffusons*, and *locons*.^[36,37] Propagons are low-frequency, wave-like modes analogous to acoustic phonons; they retain coherence and efficiently transport heat but are sparsely sampled in finite supercells. Diffusons are spatially extended but nonpropagating modes with randomized eigenvectors; they dominate the vibrational spectrum and contribute most to thermal conductivity via a diffusive mechanism.^[10] Locons are highly localized vibrations confined to small atomic clusters, contributing little to bulk transport but relevant for localized dissipation.

Following AF, we compute the thermal diffusivity D_n as^[37]

$$D_n = \frac{\pi V^2}{3\hbar\omega_n^2} \sum_{m \neq n} |S_{nm}|^2 \delta(\omega_n - \omega_m) \quad (20)$$

where V is the system volume, ω_n is the frequency of mode n , and S_{nm} are matrix elements of the heat current operator. The thermal diffusivity for the 4096-atom a-Si model is plotted as a function of vibrational energy in Figure 1a. Blue and red dashed lines delineate the spectral ranges of the three vibrational mode types: propagons (0–10 meV), diffusons (10–56.5 meV), and locons (>56.5 meV). A sharp decline in diffusivity near

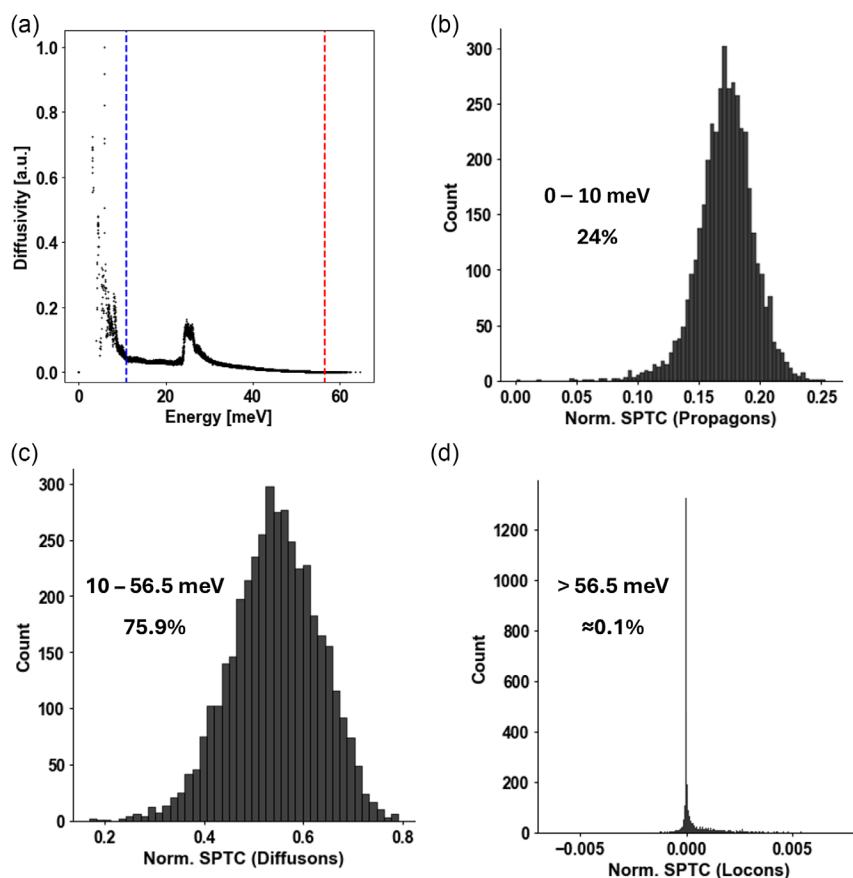


Figure 1. Vibrational mode analysis for the 4096-atom a-Si model. a) Thermal diffusivity versus vibrational energy, delineating energy regions for propagons (left of blue dashed line), diffusons (middle), and locons (right of red dashed line near the mobility edge). SPTC distributions from b) propagons, c) diffusons, and d) locons. Insets indicate their energy ranges and percentage contributions to total SPTC. Similar plot for the 512-atom a-Si model is provided in Figure S2, Supporting Information.

56.5 meV ($\approx 456 \text{ cm}^{-1}$) marks the *mobility edge*—the boundary between extended (diffuson) and localized (locon) modes, per the Allen–Feldman (AF) framework. This classification is further supported by the vibrational density of states (VDOS) in Figure S1, Supporting Information, of the Supplementary Materials, which shows strong localization in the high-frequency locon regime.

The vibrational mode-projected SPTC was computed and its distribution is shown in histograms in Figure 1b–d for propagons, diffusons, and locons, respectively. Each histogram captures the spread of the SPTC values attributed to vibrational modes within a given energy range, with insets indicating the corresponding vibrational energy window and the maximum relative contribution (in percent) to the total system SPTC—defined as the calculated values without mode-projection. The propagator and diffuson distributions are approximately Gaussian, with peak SPTC contributions near 17% and 55%, respectively. In contrast, the locon distribution is highly skewed, featuring a narrow peak at $\approx 0.1\%$ and a long tail, reflecting their highly localized nature. This analysis carried out for the 512-atom structure, shown in Figure S2, Supporting Information exhibit similar distribution pattern.

Although propagator modes constitute only $\approx 3\%$ of the VDOS, they contribute disproportionately (24%) to the total SPTC. These low-frequency, wave-like modes are particularly sensitive to system size. While the SPTC formalism itself remains valid across system sizes, the projection method effectively captures only those propagators with wavelengths commensurate with the finite dimensions of the simulation cell. Consequently, the estimated propagator contribution may be systematically underestimated in limited-size models, a limitation further addressed in Section 4.5.

The spatial distribution of SPTC for propagator modes is relatively homogeneous across the structure. This is demonstrated in Figure 2a, where atoms contributing to the top 25% of the propagator SPTC are shown with increased radius. These high-contributing atoms are broadly distributed without significant clustering: 757 atoms fall within this high-SPTC range, yet the largest connected cluster contains only 18 bonded atoms. Additional details from the clustering analysis are provided in Table S1, Supporting Information. The weak correlation with local structural motifs reinforces the interpretation that propagators facilitate a delocalized, system-wide mechanism of thermal transport.

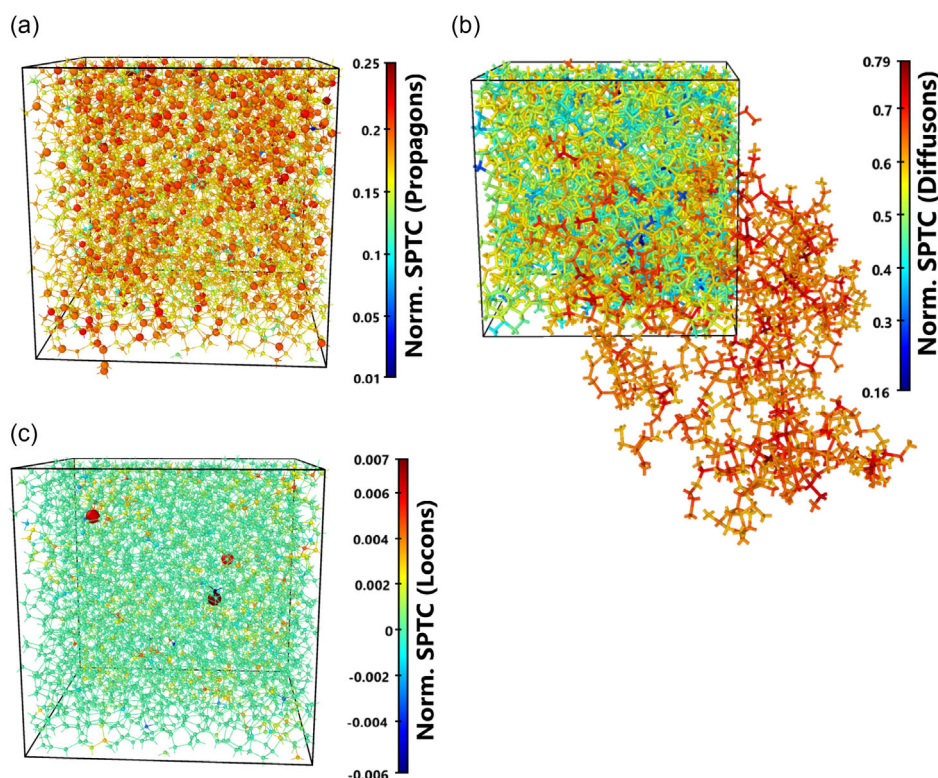


Figure 2. The contributions of a) propagons, b) diffusons, and c) locons to the total SPTC are illustrated for the 4096-atom a-Si structure. The mode-projected SPTC is color-coded, and its values are normalized by the total SPTC (i.e., without vibrational mode projection), so red regions correspond to the highest relative contributions within each mode class. Atoms contributing up to 75% of the mode's maximum SPTC (i.e., the high-SPTC range) are highlighted with increased radius, except in (b) where this is omitted for visual clarity. Atomic coordinates are unwrapped from periodic boundaries to better reveal the spatial connectivity of the top 75% contributors and their distribution throughout the simulation cell. Similar analysis for the 512-atom model is provided in Figure S3, Supporting Information.

Diffusons account for roughly 92% of the vibrational spectrum and contribute 75.9% to the total thermal conductivity. Spatial analysis of its SPTC distribution reveals significant clustering among high-contributing atoms (top 25%), as shown in Figure 2b. In this range, 1197 atoms are identified, of which 1093 form a single connected network through bonded interactions (see Table S1, Supporting Information). To illustrate this extended spatial connectivity, the atomic coordinates are unwrapped from periodic boundary conditions in the visualization. Diffusion modes with the highest SPTC values are found to correlate with local structural features, specifically bondlengths. The top 32 atoms ranked by SPTC exhibit an average bondlength of 2.39 Å, while the bottom 35 atoms (lowest SPTC) have a shorter average bondlength of 2.30 Å. For context, the overall mean bondlength in the structure is 2.34 Å. This bond-length dependence suggests that diffuson-mediated thermal transport is highly sensitive to local structural disorder and scattering strength. These observations support the interpretation of a filamentary character in heat conduction through amorphous silicon, a phenomenon that will be examined further in Section 4.7.

Finally, locons contribute a negligible $\approx 0.1\%$ to the total SPTC, with only three spatially isolated atoms accounting for up to 75% of the locon SPTC, as shown in Figure 2c. Notably, some of these contributions include negative SPTC

values, which arise as numerical artifacts due to the ill-defined nature of the heat flux for highly localized modes. These modes exhibit minimal participation in heat transport, rendering their contribution to microscopic thermal conductivity essentially insignificant.^[1,51]

The qualitative behavior of propagons, diffusons, and locons observed in the 4096-atom model is similar in the 512-atom a-Si structure. The spatial projection of the top 25% SPTC-contributing atoms for that case is provided in Figure S3, Supporting Information, and the associated clustering data are summarized in Table S1, Supporting Information.

4.2. Locality of the Force Constant Matrix \Rightarrow Spatial Locality of SPTC

The rapid spatial decay of the FCM is a well-established feature that underpins many practical lattice dynamics calculations (e.g., Ref. [52]). To gain analytical insight into this behavior, we consider in Appendix B a generic pair potential of the Lennard–Jones type,^[53] with arbitrary powers m and n where $n < m$

$$V_{LJ}(r) = \left(\frac{A_m}{r}\right)^m - \left(\frac{B_n}{r}\right)^n \quad (21)$$

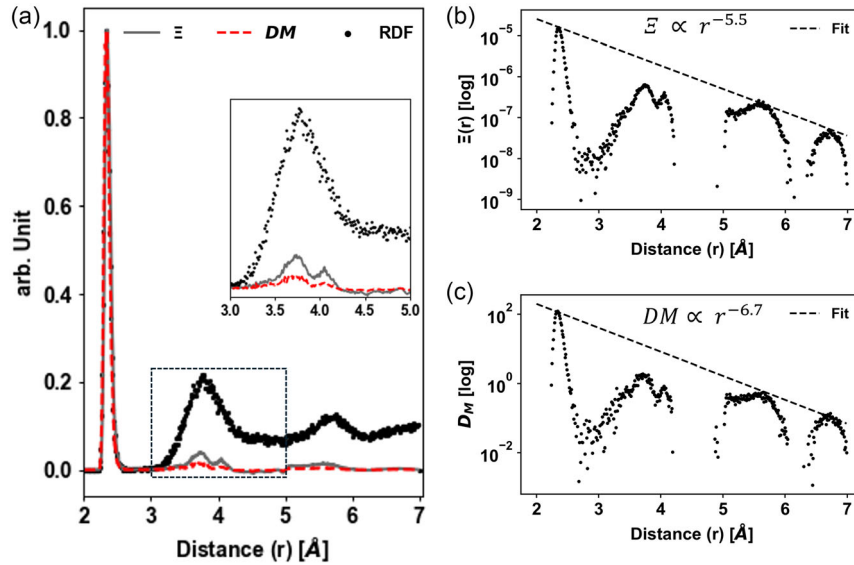


Figure 3. Spatial convergence analysis of the 4096-atom amorphous silicon model. a) Cell-averaged decay of Ξ and DM as a function of interatomic distance $r = |x - x'|$, shown alongside the radial distribution function (RDF, black) for reference. b) Semilogarithmic plot (log-scale on the y-axis) of Ξ illustrating exponential decay behavior, with a linear fit (dashed black line) indicating a decay-rate power of 5.5. c) Same as (b), but for DM, with a decay-rate power of 6.7.

and derive the asymptotic form of the FCM decay. As shown in Appendix C, the SPTC summation converges for $n > 2$, confirming the “short-ranged” interactions for a well-defined, spatially local thermal conductivity.

To assess this spatial decay empirically, we analyze the 512- and 4096-atom a-Si models. **Figure 3a** shows the decay of Ξ and DM as a function of radial distance $r = |x - x'|$, averaged over all atomic sites, for the 4096-atom a-Si. For structural context, the radial distribution function (RDF) is also plotted to highlight that both Ξ and DM decay smoothly with distance and show no significant features beyond the second or third coordination shell. The inset highlights a weak secondary peak in Ξ , with an even fainter signal in the DM.

Figure 3b,c presents the decay of $\Xi(r)$ and DM elements on a semi-logarithmic scale, revealing a power-law behavior. The extracted decay exponents are approximately 5.5 for Ξ and 6.7 for the DM, with the latter consistent with prior quantum Monte-Carlo results.^[54] We also note that the decay range of Ξ approximately aligns with the estimated phonon mean free path, $l \approx 8 \text{ \AA}$.^[2]

A corresponding analysis for the 512-atom a-Si model is provided in Figure S4, Supporting Information, which shows consistent peak positions and decay profiles compared to the 4096-atom system. Notably, the decay power for Ξ remains at 5.5, while the decay exponent for DM decreased slightly to 6.1.

4.3. The Spectrum of Ξ

The eigenvectors of Ξ are helpful for identifying the most and least conducting parts of the network. We diagonalized Ξ and present its density of states (DOS) and corresponding inverse participation ratio (IPR) in the top panel of **Figure 4**, for the 4096-atom a-Si model. We note that the eigenvectors (η) of Ξ

are mostly extended excepting those conjugate to the most negative eigenvalues, λ (see Equation 10). To study this spatially, the atoms contributing to the (de)localization for nine representative eigenvalues (labeled “a–i” in Figure 4) from three distinct regions were projected, and one mode from each region is shown in the lower panel of Figure 4 (labeled b, e, and h). The remaining six representative eigenvectors are provided in Figure S5, Supporting Information.

The first region (a, b, c), near the left band edge, exhibits spatially localized modes that form compact clusters (small blobs) composed of atoms with high SPTC (see color bar for scale). In contrast, the second region (d, e, f), where $\lambda \approx 0$ features extended modes, predominantly involving atoms with low to intermediate SPTC. The third region (g, h, i), characterized near the right band edge, also includes interconnected atom clusters with high SPTC values, which we will correlate with our segmentation analysis in Section 4.7. Moreover, we find that a small fraction of the modes constitute most of the thermal conduction (these are modes near the high- λ edge).

To partly address this, we present the contributions of the eigenvectors η_μ (and their corresponding eigenvalues λ_μ) to the mode-projected conductivity, κ_μ (see Equation 12), as shown in **Figure 5a** (black scatter). Four distinct regions (i–iv) are identified based on their contributions to the total conductivity, $\kappa \approx 0.85 \text{ W m}^{-1} \text{ K}^{-1}$: (i, blue) The region with all negative eigenvalues ($\lambda_\mu < 0$), contributing 19% to κ ; (ii, red) A set of low-positive eigenvalue modes ($0 < \lambda_\mu \lesssim 1.0 \times 10^{-4}$) which all yield negative values for 19%, offsetting κ by roughly 9.4%; (iii, yellow) a transitional region ($1.0 \times 10^{-4} < \lambda_\mu \lesssim 1.9 \times 10^{-4}$) containing both negatively (5.2%) and positively (7%) κ_μ values; and (iv, green) the dominant region ($\lambda_\mu > 1.9 \times 10^{-4}$), where all modes have positive values of κ_μ and contribute accounts for $\approx 88\%$ of κ .

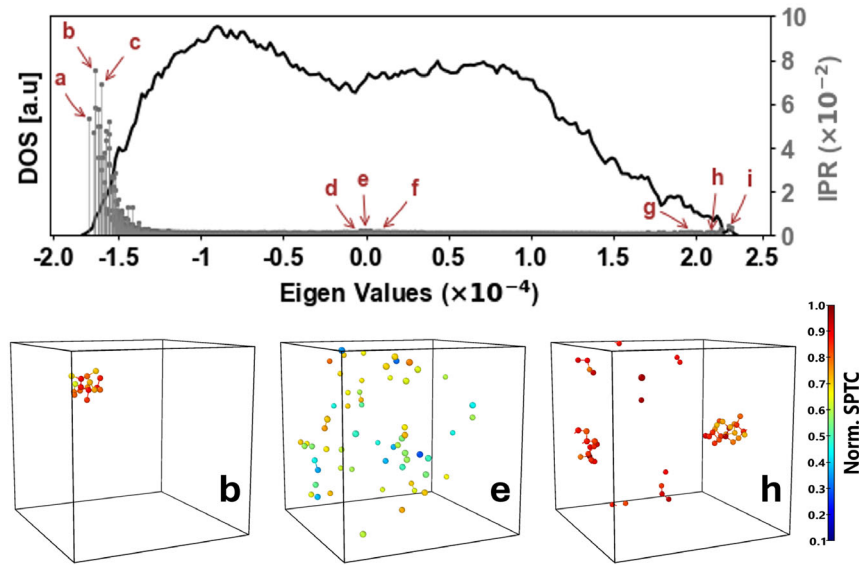


Figure 4. The top panel shows the density of states (DOS; black) and inverse participation ratio (IPR; gray) of the Ξ matrix for the 4096-atom a-Si structure. Nine representative eigenvalues (a–i) are selected from three distinct spectral regions and are highlighted. The atomic configurations corresponding to modes b, e, and h are shown in the lower panel, with atoms color-coded by their SPTC contributions. Visualizations for the remaining highlighted eigenvalues, along with the DOS and IPR plots for the 512-atom structure, are provided in Figure S5, Supporting Information.

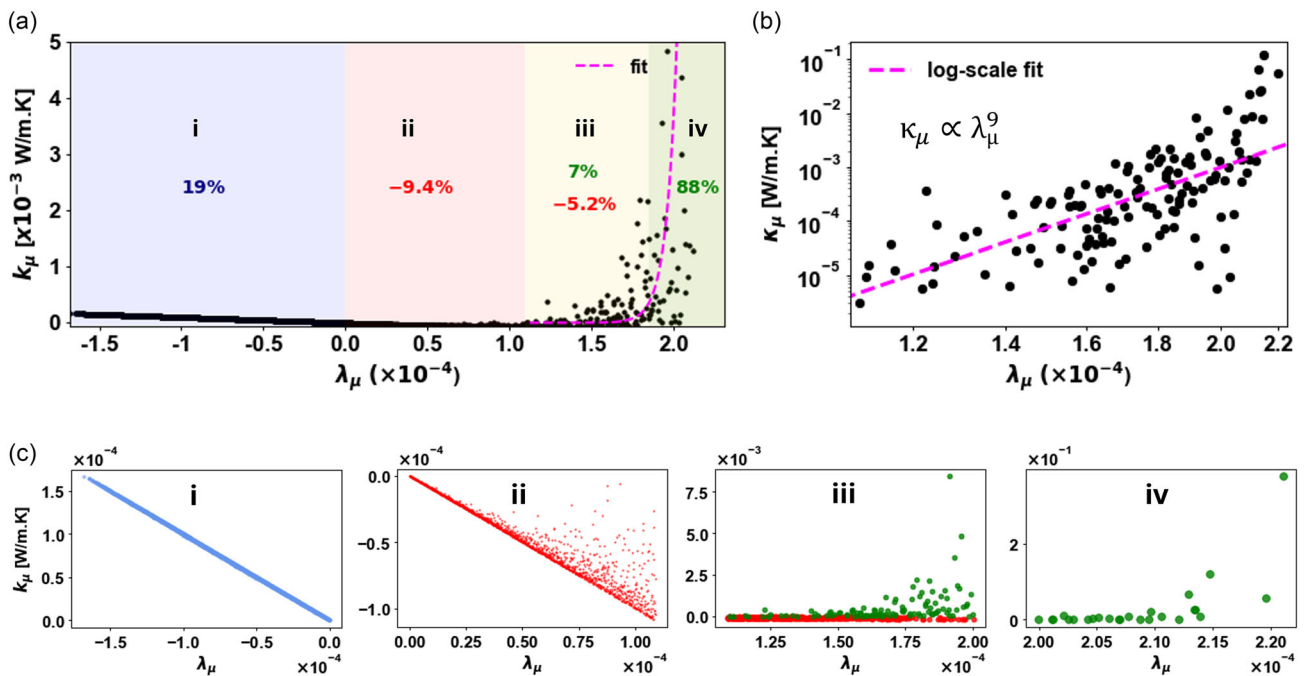


Figure 5. Mode-projected thermal conductivity, κ_μ , for the 4096-atom a-Si structure. a) The black scatter plot show κ_μ plotted against the eigenvalues (λ_μ) of contributing eigenvectors, η_μ . Colored bands highlight four distinct regions, i (blue)–iv (green), of κ_μ contribution to the total conductivity κ ($\approx 0.85 \text{ W m}^{-1} \text{ K}^{-1}$). The percentage contribution from each region is indicated by color, except in the yellow region (iii), which represents the combined contributions of the $-\kappa_\mu$ red (ii) and all $+\kappa_\mu$ green (iv) regions. b) The power-law fit (magenta, dashed line) from the green and yellow region in (a) is replotted on a doubly logarithmic scale, revealing a decay power of 9.0. c) Scatter plots i–iv show κ_μ versus λ_μ for the four regions, using their assigned colors for identification.

A roughly power-law decay trend (magenta dashed line) is observed in the green-to-yellow region of Figure 5a. When plotted on a doubly logarithmic scale (Figure 5b), this trend reveals a decay power of ≈ 9.0 . The scatter plots in Figure 5c (i–iv), color-coded by region, highlight the relationship between κ_μ and λ_μ for each contributing subset. Notably, the blue and red regions contain 2,100 and 1,438 modes, respectively. The yellow region comprises 422 negatively contributing modes and 111 positively contributing modes. In contrast, the dominant green region includes only 25 modes. These results suggest that thermal transport in a-Si is primarily governed by a small number of quasi-extended modes with large κ_μ , while the majority of modes either contribute minimally or act destructively, offsetting the net conductivity.

This large κ contribution from the modes in the large- λ tail in the green region is reminiscent of the electronic version of this work in which we found that electronic conduction was determined by a tiny subspace of the full space of the eigenvectors of Γ .^[24] For electrons, Γ is positive semi-definite so that the non-contributing modes were concentrated at $\Lambda = 0$, whereas for thermal transport modes at the positive spectral edge dominate. For the electronic case, there was a “tail” in the density of states of Γ near $\Lambda = 0$ only for the case of a metal (Al); for the thermal case (a-Si), a narrow power-law tail is observed near the right band edge in the distribution of κ_μ (Figure 5a).

4.4. Convergence of SPTC with Respect to Broadening and Spatial Cutoff

In the SPTC formalism, the δ function in Equation 7 is approximated by a Lorentzian function^[37]

$$\delta(\omega) = \frac{\varepsilon}{\pi(\omega^2 + \varepsilon^2)} \quad (22)$$

The influence of the Lorentzian broadening parameter, ε , on the computed thermal conductivity (κ) is shown in Figure 6a. We observe that κ reaches a maximum near $\varepsilon = 2$ K (in temperature units), and gradually decreases with further broadening. Based on this behavior, we adopt $\varepsilon = 2$ K as the default value for all SPTC calculations in this work. This choice aligns with the

broadening factor η used in previous studies by Allen and Feldman.^[37]

In addition, the decay of $\Xi(r)$ with interatomic distance enables spatial truncation radius, R_c , to limit the computational cost. For a-Si, a conservative choice of $R_c \approx 7.0$ Å is sufficient to capture the relevant physics. This is demonstrated in Figure 6b, which shows the convergence of the SPTC for atomic sites with the maximum (blue) and minimum (red) contributions in the 512-atom a-Si model. Both curves plateau within the range of 6–7 Å, implying the adequacy of this spatial cutoff. Consequently, for a fixed tolerance (degree of convergence of the SPTC for a given site), one only need contributions to a given site R due to sites within a radius R_c of R . Thus, it is easy to compute the SPTC in a linear scaling fashion,^[55–58] once the DM has been diagonalized.

4.5. Finite-Size Effects

The effects of system size on SPTC of a-Si were assessed by comparing the fractions carried by propagons, diffusons, and locons for supercells containing 64, 216, 512, and 4096 atoms. In Table 1 and Figure 7a, the propagon contribution grows monotonically from 0.15% at $N = 64$ to 24% at $N = 4096$. This increasing trend of propagon contributing has also been reported for simulations carried out via the normal mode decomposition method,^[22] and the contribution at $N = 4096$ is fairly close to the lower limit of 28% reported in frequency-domain thermoreflectance measurements for a-Si thin films.^[59]

Concomitantly, the contribution from diffusons decreases from 99.8% to 75.9% as system size increased (Figure 7b), mirroring the inverse propagon–diffuson correlation reported in

Table 1. Contributions of vibrational modes to SPTC and thermal conductivity (κ) in a-Si for different system sizes.

No. of atoms	Propagons [%]	Diffusons [%]	Locons [%]	κ [W m ⁻¹ K ⁻¹]
64	0.15	99.81	0.04	0.55
216	10.73	89.17	0.10	0.65
512	15.29	84.63	0.08	0.88
4096	24.02	75.93	0.04	0.88

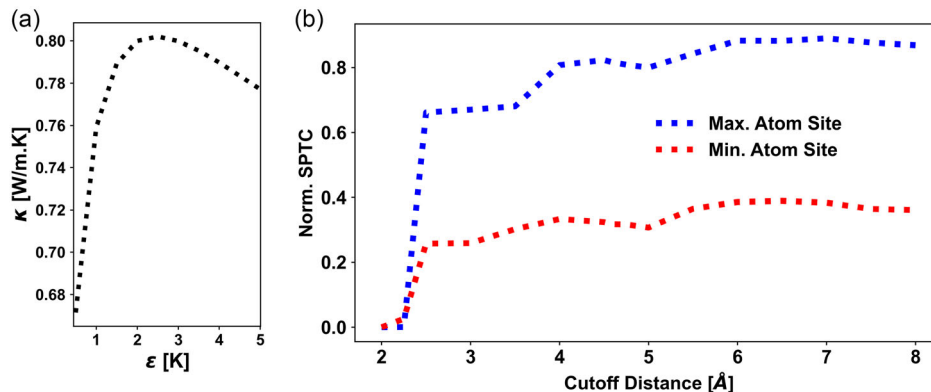


Figure 6. a) Dependence of the computed thermal conductivity (κ) on the Lorentzian broadening factor (ε). b) Convergence of site-projected thermal conductivity (SPTC) with respect to the spatial cutoff radius R_c , shown for the atomic sites with the highest (blue) and lowest (red) SPTC values. Results are shown for the 512-atom a-Si model.

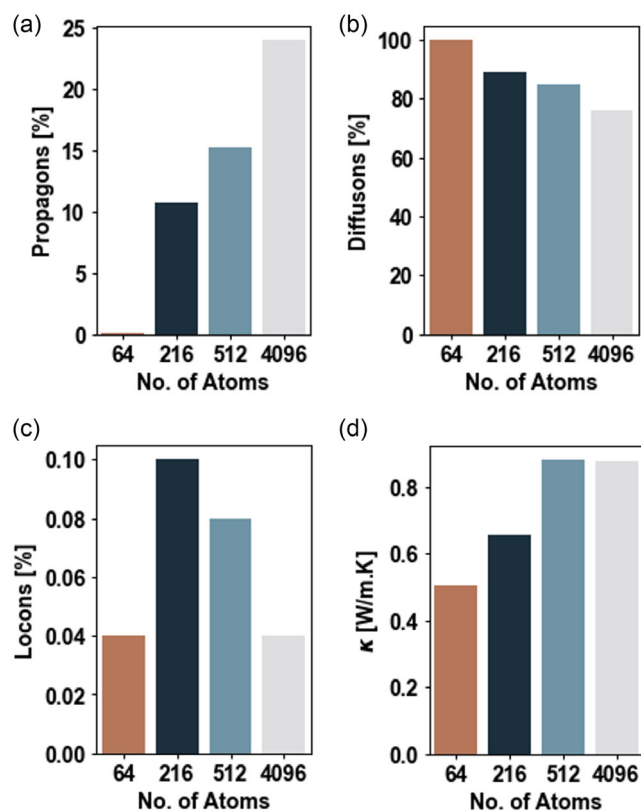


Figure 7. Size effects on SPTC calculations. Histograms showing the percentage contribution to the total SPTC from a) propagons, b) diffusons, and c) locons for a-Si across four different system sizes. The corresponding trend in total thermal conductivity (κ) with increasing system size is shown in (d).

time-domain thermoreflectance measurements on a-Si films.^[60] Locons remain below 0.1% for every size considered (Figure 7c), consistent with the AF picture that locons are spatially localized and therefore ineffective heat carriers.^[1]

The overall thermal conductivity, κ , rises from 0.55 to 0.88 Wm⁻¹ K⁻¹ between 64 and 512 atoms but then appears to saturate for 4096 atoms (It is of some interest that our results for diffusivity and thermal conductivity are in fairly close agreement with FKA. Our models were of the same WWW-type, but we used the accurate GAP potential to handle the interatomic interactions. The results were similar enough to suggest that the details of the potential *may not* play a large role for thermal transport.) (Figure 7d). A similar plateau emerges once the sample thickness exceeds the longest propagon mean-free paths in both thermoreflectance experiments^[60] and non-equilibrium molecular-dynamics simulations of a-Si.^[22] This then suggests that total heat transport and SPTC is governed by a balance between long-range propagons—whose contribution is limited by boundary scattering once their mean free paths exceed the box size—and short-range diffusons, whose diffusive character dominates the residual conductivity when propagons are fully scattered.^[12]

4.6. Anharmonic Effects

To assess the anharmonic contributions to thermal conductivity, which are not captured by the harmonic approximation employed in the SPTC formalism (Equation 9), we computed the thermal conductivity of the 512-atom a-Si model using the Green–Kubo (GK)^[23,31] formalism from molecular dynamics (MD). In this approach, the thermal conductivity is obtained from the ensemble average of the heat current autocorrelation function (HCACF), given by^[23,31,61,62]

$$\kappa_{\text{MD}} = \frac{1}{3Vk_B T^2} \int_0^\tau \langle \mathbf{J}(0) \cdot \mathbf{J}(t) \rangle dt \quad (23)$$

where V is the system volume, T the temperature, and k_B is Boltzmann's constant. The upper limit of integration, $\tau = 1$ ns, approximates the correlation time beyond which the heat flux autocorrelation function decays to zero. A Nosé–Hoover thermostat^[63,64] was used to thermalize and equilibrate the system at $T = 300$ K under microcanonical/constant volume (NVT) conditions, using a 1 fs time step. The equilibrated atomic velocities were subsequently used in a microcanonical (NVE) ensemble to obtain the HCACF.

The total thermal conductivity obtained from the Green–Kubo method was found to be 0.75 W m⁻¹ K⁻¹, while the harmonic phonon-based SPTC approach yielded a value of 0.88 W m⁻¹ K⁻¹. The $\approx 15\%$ difference in conductivity values is most likely due to the neglect of anharmonic effects in the harmonic SPTC formulation.^[65,66] However, both values are consistent with experimental measurements at room temperature,^[21] indicating that anharmonic effects, though present, do not drastically alter the thermal conductivity in a-Si. This result supports the validity of the harmonic approximation as a reasonable framework for capturing the dominant mechanisms of thermal transport in a-Si.

4.7. SPTC for Amorphous Silicon

In this section, we investigate the underlying structural configurations that may serve as preferential channels for thermal energy flow in a-Si. The observed transport behavior is predominantly governed by diffusion modes, as discussed in Section 4.1.

Although the spatial distribution of SPTC in the a-Si models appears random at first glance, segmentation of the network into three conductivity-based sub-networks: low (10–50%), intermediate (50–75%), and high (>75%), reveals emergent spatial organization. These sub-networks are visualized in the top row of **Figure 8a** for the 4096-atom configuration, with the full SPTC range spanning 10%–100% (see enlarged view in Figure 8c). Notably, the lowest SPTC values remain finite: 32% and 10% for the 512- and 4096-atom system, respectively (see **Table 2**). This indicates that atoms in low-conductivity regions still contribute non-negligibly to the overall thermal response. The selected SPTC thresholds are informed by characteristic features in the RDF (bottom row of Figure 8a), as well as by correlations between SPTC and local energetic and structural metrics (Figure S6a,b, Supporting Information).

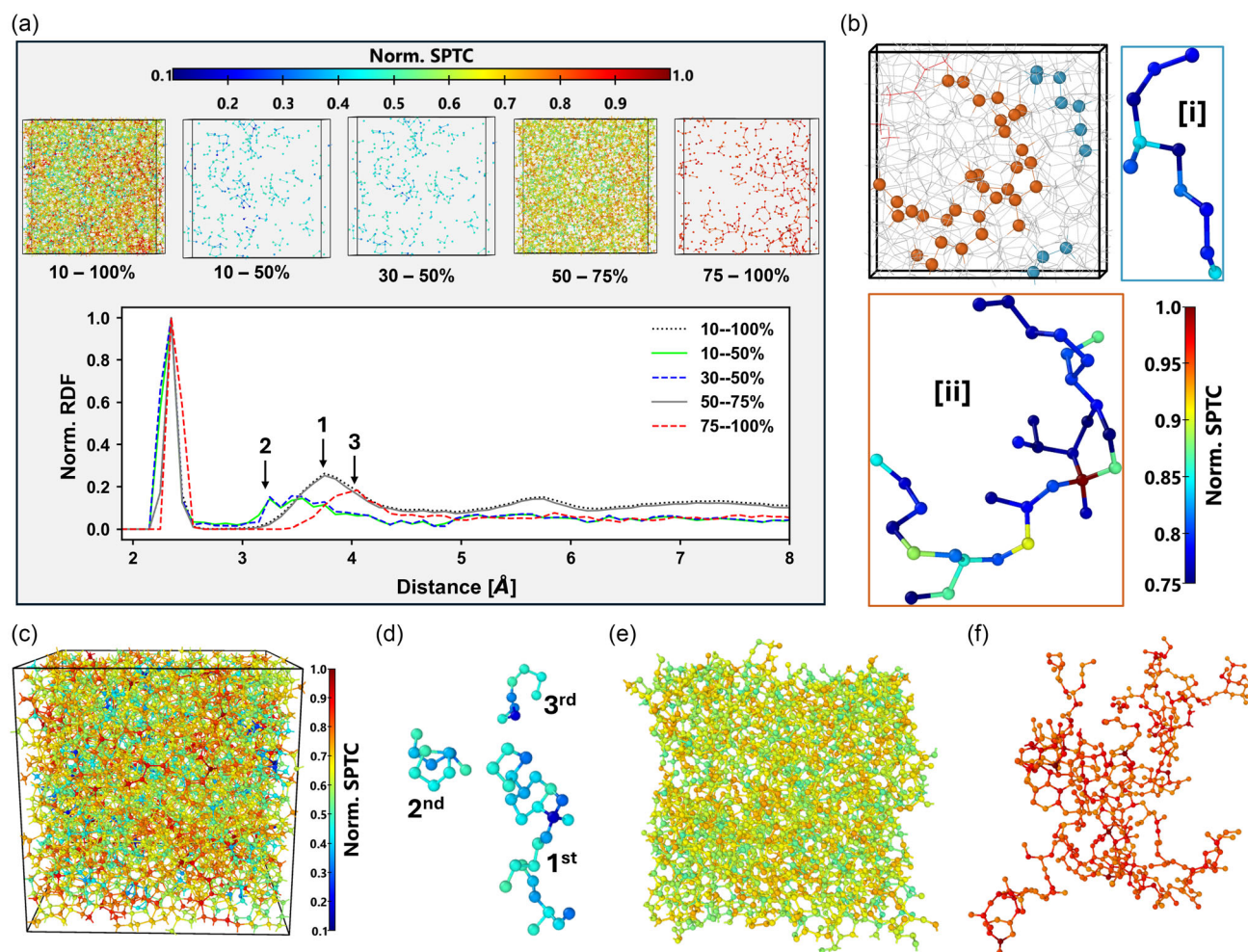


Figure 8. SPTC analysis for two a-Si models containing 512 and 4096 atoms. a) (Top) Spatial distribution of SPTC in the 4096-atom model segmented by range, with corresponding normalized radial distribution functions (RDFs). b) High-SPTC filaments (SPTC > 75%) in the 512-atom model, with blue and brown filaments highlighted in panels (i) and (ii), respectively. c) Full SPTC map across atomic sites in the 4096-atom model. Visualization of d) the first, second, and third low-SPTC filaments 10%–50%; e) the largest midrange SPTC cluster 10%–50%; and f) the longest high-SPTC filament in the structure. Clusters in (d)–(f) are color-mapped by SPTC value.

Table 2. Cluster analysis for different SPTC ranges in the 512- and 4096-atom a-Si structures. Clusters are ranked from first (1st) to eighth (8th) largest in size. A cluster consists of at least two bonded atoms. \overline{BL} denotes the average bondlength within each cluster.

512-Atom amorphous silicon											
SPTC range [%]	No. of atoms	\overline{BL} [Å]	1st	2nd	3rd	4th	5th	6th	7th	8th	Filament?
32–50	73	2.28	15	13	6	6	5	4	2	2	Yes
50–75	76	2.34	375	–	–	–	–	–	–	–	No
75–100	63	2.39	32	10	6	3	2	2	–	–	Yes
4096-Atom amorphous silicon											
10–50	366	2.30	26	10	8	8	7	7	7	7	Yes
50–75	2815	2.34	2792	3	2	2	–	–	–	–	No
75–100	915	2.39	496	48	37	21	19	17	16	16	Yes

The RDF of the 4096-atom model reveals three distinct second-neighbor peaks (labeled “1,” “2,” and “3”) associated with different SPTC intervals. Peak “1” corresponds to both the full

system and the mid-SPTC range, centered near the expected second-neighbor distance of 3.75 Å.^[50] In contrast, peak positions shift to 3.45 and 4.05 Å for the low- and high-SPTC groups,

respectively. These deviations provide physical justification for the segmentation thresholds. As shown in Table 2, a majority of atoms belong to the mid-SPTC category $\approx 73\%$ and 69% for the 512- and 4096-atom models, respectively—consistent with the dominant contribution of this regime to the bulk structure and RDF profile.

The topology of these sub-networks is also of interest. Quantitative metrics for the subnetworks are provided in Table 2, including atom counts, cluster or filament sizes based on nearest-neighbor bond connectivity, and morphological classification. High-SPTC atoms tend to be part of extended, filamentary structures, as illustrated in Figure 8b, which highlights the two longest “hot” filaments in the 512-atom model, colored i) blue and ii) brown. In the 4096-atom model, the largest high-SPTC cluster (Figure 8f) contains 496 atoms and exhibits a more entangled, less linear morphology, reminiscent of polymer chains in high-density polyethylene.^[67] Additionally, the contributing atoms to the high-SPTC segment are primarily those associated with the extreme values of the eigenvalue spectrum, as discussed in Section 4.3.

By contrast, low-SPTC atoms form small blobs, with the largest one containing only 26 atoms (see Figure 8d). The mid-SPTC group represents the structural backbone: in the 4096-atom system, 2792 out of 2815 atoms form a single bond-connected network (Figure 8e). These observations suggest that high-SPTC filaments are embedded within the amorphous network and form a percolating substructure for thermal transport. These filaments are spatially extended and form percolating, space-filling networks throughout the supercell under periodic boundary conditions. This spatial continuity is evident in the visualization of the longest filament in the 4096-atom system, shown in Figure S7, Supporting Information.

The average bondlength (\overline{BL}) for the subnetworks in Table 2 exhibit correlation with the SPTC ranges. \overline{BL} increases progressively from the low- to high-SPTC subnetworks. In particular, the low-SPTC subnetworks exhibit shorter average bondlengths of 2.28 and 2.30 Å for the 512-atom and 4096-atom models, respectively. By contrast, the mid- and high-SPTC subnetworks show a consistent \overline{BL} of 2.34 and 2.39 Å in both systems. The increasing bondlength in high-SPTC structures could indicate enhanced vibrational coherence, consistent with their role in facilitating heat transport.

There are two key observations regarding the bonding environment. First, the \overline{BL} associated with the SPTC subnetworks closely match those obtained for diffusion modes, strongly suggesting that diffusions dominate the SPTC contributions. Second, the bond connectivity within the low- and high-SPTC subnetworks exhibits a structural self-correlation: Short bonds preferentially connect to other short bonds, and similarly for long bonds, consistent with earlier findings.^[68,69]

We draw the readers attention to another point of potential interest. The role of filaments in thermal conduction is reminiscent of prior works by Pan et al.^[70] and Drabold et al.^[71] concerning Urbach tails,^[72] which revealed that the valence tail states in a-Si are associated with connected short bonds, while the conduction tail states correspond to long bonds in a filamentary structure. Electronic conduction in the material is affected by the blob-filament characters of the Urbach tail because of its

proximity to the Fermi level.^[73,74] Analogously, in the thermal case, we find that short bonds are predominantly involved in the low-SPTC subnetwork, whereas long bonds dominate the high-SPTC structures. This correspondence indicates a structural correlation between the local bonding environment and both the electronic and thermal transport properties of a-Si. Work is underway to determine to what degree the same filaments or blobs contribute to electrical and thermal processes. It is of considerable interest to understand the similarities and differences of thermal and electronic defects.

5. Other Applications

5.1. An Amorphous-Crystal Interface in Silicon

Grain boundaries and interfaces play a significant role in governing the electronic and thermal properties of materials. Previous studies have shown that grain boundaries in silicon and tungsten can reduce SPTC by up to 30%.^[13,75] Here, we examine the impact of amorphous–crystalline (a–c) interfaces on thermal transport using a silicon sandwich structure modeled after Feldman and Bernstein.^[76]

An initial 1000-atom amorphous Si structure was generated via molecular dynamics using the environment-dependent interatomic potential (EDIP),^[77] by melting crystalline Si, quenching to 1000 K, and annealing. The resulting structure was duplicated and trimmed to create a 1222-atom amorphous slab, which was combined with an 800-atom crystalline Si slab oriented along the $\langle 100 \rangle$ direction. The composite was then relaxed and annealed at 1000 K under periodic boundary conditions.

To improve energetic accuracy, the structure was further annealed at 300 K using the Gaussian Approximation Potential (GAP)^[29] in LAMMPS,^[42] reaching a stable density of 2.285 g cm^{-3} . The transition from EDIP to GAP reduced the energy by $\approx 0.036 \text{ eV}$ per atom, with minimal structural changes, indicating that EDIP provided a reasonable starting configuration.

Figure 9a (top) shows the final amorphous–crystalline (a–c) silicon structure, with atomic environments color-coded by structural type using the method of Ref. [78] as implemented in OVITO.^[79] Atoms are classified as amorphous Si (gray), cubic diamond (brown), or hexagonal diamond (green), along with their first (1-NN) and second (2-NN) nearest neighbors. Here, 1-NN (2-NN) denotes atoms at crystalline sites adjacent to non-crystalline second (first) neighbors. While the crystalline domain predominantly retains its cubic diamond structure, some interfacial atoms adopt the hexagonal diamond configuration to accommodate local structural mismatch.

As summarized in Table 3, the number of atoms in the amorphous and cubic diamond regions decreases from 1222 and 800 to 1085 and 625, respectively, after interface relaxation. The normalized SPTC per atomic site, shown in the lower panel of Figure 9a, is represented as a colormap ranging from blue (low SPTC) to red (high SPTC). Atoms in the bulk crystalline region exhibit the highest SPTC values ($\rightarrow 1$), which gradually decline across the a–c interface (red \rightarrow yellow \rightarrow green), where values are significantly lower. This profile captures the reduction in thermal activity as heat propagates from the ordered crystalline phase into the disordered amorphous region.

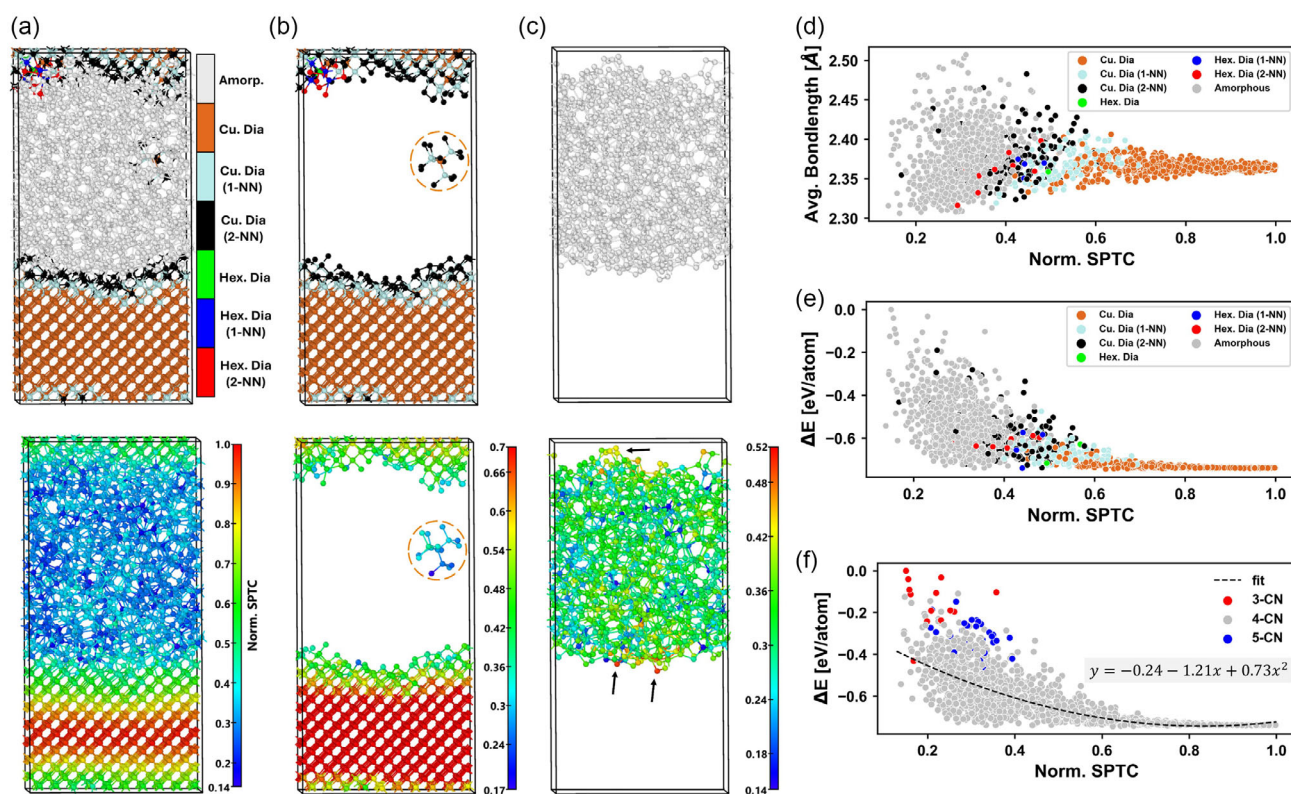


Figure 9. SPTC analysis of the amorphous-crystal interface in silicon. (a, top) Atomic configuration with color-coded structural classification: amorphous (Amorp.; gray), cubic diamond (Cu. Dia; brown), and hexagonal diamond (Hex. Dia; green), including first (1-NN) and second (2-NN) nearest neighbors (NN). The top panels of (b) and (c) delineate the crystal-like and amorphous regions, respectively. The lower panels of (a)–(c) show the normalized SPTC values per atom (blue, low; red, high). d) Relationship between SPTC, structure type, and per-atom average bondlength. The relationship between SPTC and phenomenological GAP site energy difference (ΔE) is shown in (e) as a function of structure type and in (f) as a function of coordination number (CN). The black curve in (f) shows a quadratic fit, with the equation provided in the inset, and atoms are color-coded by coordination: 3-CN (red), 4-CN (gray), and 5-CN (blue).

Table 3. SPTC statistics across structural types in the amorphous-crystalline sandwich Si structure.

Structure	No. of atoms	Max [%]	Mean [%]	Min [%]
Cubic Dia.	625	100	81	42
1-NN	151	70	53	34
2-NN	146	61	42	25
Hexagonal Dia.	2	57	53	49
1-NN	4	49	45	43
2-NN	9	48	38	29
Amorphous	1085	52	31	14

To isolate the spatial distribution of SPTC within each structural domain, Figure 9b,c presents the crystalline and amorphous regions separately. In Figure 9b, the colormap is truncated at the maximum SPTC value among cubic diamond 1-NN atoms ($\approx 70\%$ of the bulk value; see Table 3), revealing a spatial distribution consistent with the structural classification. Figure 9c shows the amorphous region, where the SPTC reaches a maximum of roughly 52% of the bulk value, with peak values localized near the interface, as indicated by black arrows.

Figure 9d highlights the correlation between SPTC and the local bonding environment. Atoms with the highest SPTC exhibit interatomic distances near ≈ 2.36 Å, corresponding to the equilibrium Si–Si bondlength in the crystalline phase. Since structural identity is partly determined by bondlengths (with bond angles also playing a role), high-SPTC atoms are predominantly found in the cubic diamond region, followed by contributions from hexagonal diamond configurations and their nearest neighbors. In contrast, atoms in the amorphous region display a broader distance distribution and consistently lower SPTC values, indicative of a disordered bonding network.

This observation prompts a fundamental question: *What governs the spatial variation in SPTC?* While a clear decline is observed from crystalline to amorphous domains, the transition is continuous—there is no sharp drop in SPTC at the interface. This suggests that local structural disorder gradually disrupts heat transport. However, because bondlengths and other structural metrics vary smoothly across disordered regions, direct correlation with SPTC is nontrivial. A promising approach is to use local atomic energy as a surrogate descriptor, offering a physically motivated link between structural disorder and variations in thermal conductivity.

Figure 9e,f explores the relationship between site-resolved SPTC and local atomic energy, defined as ΔE —the deviation of each atom's energy from the maximum site energy, as obtained from the GAP potential. In Figure 9e, atoms are grouped by structural classification, while in Figure 9f, coordination number (CN) is used as the grouping metric.

As seen in Figure 9e, atoms in the cubic diamond lattice exhibit low energies and high SPTC, whereas atoms in the amorphous phase are generally higher in energy and display reduced SPTC. Atoms with alternative crystalline labels occupy intermediate regions in both metrics. In contrast, when grouped by CN (Figure 9f), the energy–SPTC relationship is less distinct, especially for fourfold coordinated atoms. While threefold and fivefold atoms consistently show higher energy and lower SPTC, the broad distribution among fourfold coordinated atoms blurs any clear trend—likely due to the coexistence of both ordered and disordered environments within this category.

A more nuanced understanding emerges when both structural labels and CN are considered. For instance, black points in the low-energy, high-SPTC region of Figure 9e correspond to “2-NN cubic diamond” atoms but are spatially separated from the main cluster of such atoms. These outliers, highlighted by the brown dashed circle in Figure 9b, reside within an isolated crystalline subdomain embedded in a largely amorphous matrix. Their anomalous energetic and thermal behavior reflects nonlocal environmental effects not captured by CN or structural classification alone.

The black dotted curve in Figure 9f represents an empirical quadratic fit to the energy–SPTC data across all environments. However, within the amorphous regime (SPTC \lesssim 52%), a clear linear correlation emerges with a slope of -0.7 . This trend is consistent with observations in bulk a-Si models: for example, in the 4096-atom amorphous structure, atomic energy correlates linearly with SPTC (slope: -0.41 ; see Figure S6a, Supporting

Information), and average bondlength exhibits a similar linear relationship (slope: 0.10; see Figure S6b, Supporting Information).

5.2. A Silicon-Oxygen System

Next, we examine the thermal activity in a binary Si system, specifically non-stoichiometric silicon oxygen structures, i.e., silicon suboxide ($\text{SiO}_{x<2}$), a material identified as a promising candidate for secure storage devices due to its tunable electronic properties.^[80]

The thermal active sites in three $\text{SiO}_{x<2}$ structures, obtained from Ref. [80] is shown in Figure 10 for (a) $\text{SiO}_{1.3}$, (b) $\text{SiO}_{1.5}$, and (c) $\text{SiO}_{1.7}$, consisting of 70, 74, and 80 Si atoms, respectively. The top row illustrates atomic structures, with large brown spheres representing Si atoms and smaller red spheres representing O atoms, while the bottom row maps the SPTC per atom to a color scale ranging from blue (low) to red (high).

Unlike the electronic case discussed in Ref. [80] where active conduction pathways were identified in Si–Si connected regions, the thermal response in $\text{SiO}_{x<2}$ reveals spatially localized “thermal hotspots.” These are highlighted in Figure 10d, where Si-rich regions with prominent Si–Si bonding (labeled I and II) exhibit the highest SPTC values. In contrast, region III, similar to the silica-like environment of SiO_2 , shows the lowest thermal activity, with Si atoms predominantly bonded to oxygen. Notably, the Si–Si bonded regions facilitate electronic and thermal transport in silicon suboxide.

5.3. Carbon-Based Materials

Shifting focus to carbon-based systems, we examine the thermal response of various carbon nanostructures and the influence of

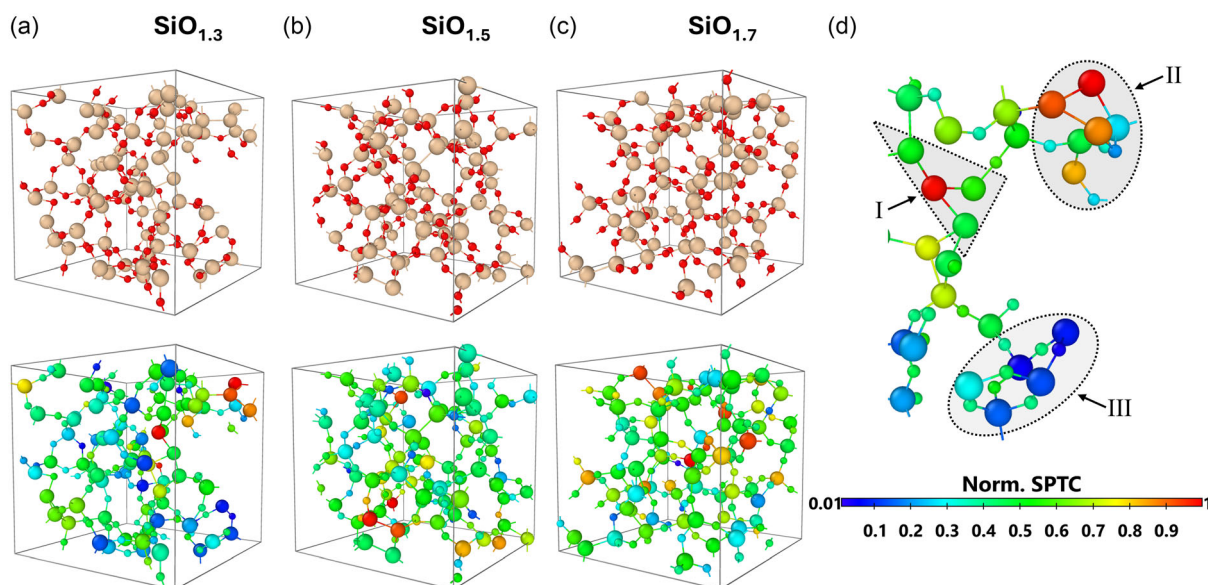


Figure 10. SPTC of silicon suboxides (SiO_x) with O concentrations of a) 1.3, b) 1.5, and c) 1.7. Si and O atoms are shown as large brown and small red spheres in the top row. The bottom row depicts the normalized SPTC values using a colormap from blue (low) to red (high). Thermal activities in Si-rich regions are highlighted in (d), with labeled regions I, II, and III in (d) indicating areas of interest.

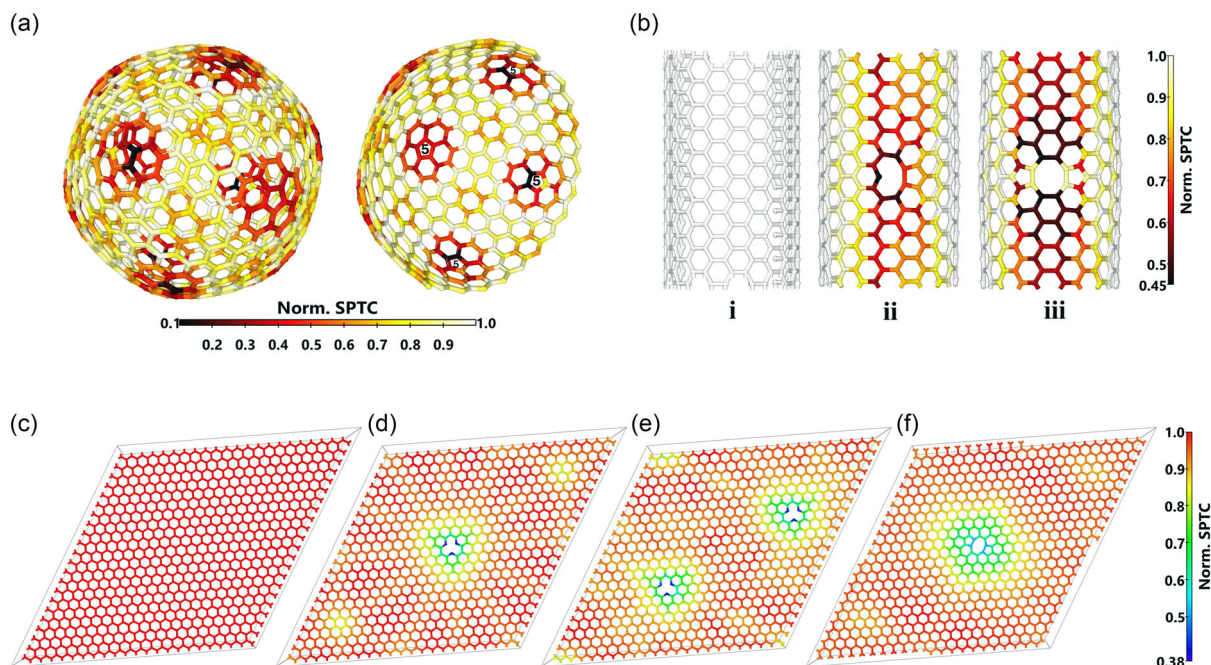


Figure 11. Thermal response visualizations for various carbon nanostructures: a) A 720-atom fullerene model, highlighting five-membered rings in one hemisphere using black labels. b) A 400-atom carbon nanotube with i) pristine structure, ii) a single vacancy, and iii) a vacancy pair. c) A 968-atom graphene model, with vacancy configurations including d) a single vacancy, e) two spatially separated vacancies, and f) a vacancy pair. Color bars represent SPTC values for each structure.

topological defects such as five-, seven-, and eight-membered rings. The thermal activity in a 720-atom fullerene model is presented in **Figure 11a**. A defining characteristic of fullerene is the incorporation of five-membered rings (pentagons) between hexagons, introducing a positive Gaussian curvature that allows its stable and spherical geometry.^[81] One could interpret this as a closed 2D system. The SPTC projection onto atomic sites, as indicated by the colorbar, reveals that regions containing pentagons exhibit noticeably reduced thermal activity.

However, one could argue that the reduced SPTC observed in fullerenes is a direct consequence of curvature rather than the presence of pentagons. To investigate this, we examined carbon nanotubes—another curved carbon allotrope. Unlike fullerenes, carbon nanotubes are composed exclusively of hexagonal rings, formed by rolling a graphene sheet into a cylindrical structure.^[82] As shown in **Figure 11b(i)**, the thermal activity across all atomic sites, including those on the curved surface, reaches the maximum SPTC value (normalized to 1).

The introduction of topological defects, namely a single vacancy and a vacancy-pair, shown in **Figure 11b(ii)** and **(iii)**, respectively, leads to a reduction in thermal activity along the defect sites. In the single vacancy case, the SPTC in the defect region decreases to $\approx 45\%$ – 50% of the maximum bulk value. In contrast, the 5–8–5 defect configuration—arising from a vacancy pair—exhibits higher SPTC values ($\approx 75\%$) on the atoms connecting the five- and eight-membered rings.

It is well established that the positive Gaussian curvature introduced by a five-membered carbon ring can be offset by the negative curvature associated with seven- or eight-membered rings.^[81–87] Consequently, topological connections between such

ring types (e.g., 5–7 or 5–8 pairs) tend to favor the formation of more planar or low-curvature nanostructures. The 5–8–5 configuration shown in **Figure 11b(iii)** exemplifies this curvature compensation mechanism, promoting localized planarity in the nanotube. We propose that the elevated SPTC values observed at the connecting atoms arise from this planar contribution. This hypothesis is further supported by analysis of a pristine 968-atom graphene model presented in **Figure 11c**, as well as the effects of vacancy-induced defects shown in **Figures 11d–f**.

Analogous to the pristine nanotube, all atomic sites in the defect-free graphene lattice composed of hexagonal rings (**Figure 11c**) exhibit maximal SPTC values, indicative of spatially uniform thermal activity. The introduction of a single vacancy (**Figure 11d**) or spatially isolated vacancies (**Figure 11e**) reveals a highly localized thermal response, consistent with the spatial decay of the DM (see Section 4.2).

This localization becomes particularly evident when comparing the SPTC associated with the 5-8-5 defect—a characteristic reconstruction of a divacancy—in both nanotube and graphene systems (**Figure 11f**). In the nanotube, the inherent curvature allows the lattice to accommodate the defect while preserving structural coherence locally. In contrast, the flat geometry of graphene lacks such adaptive flexibility, leading to a substantial suppression of SPTC values—down to $\approx 40\%$ of the bulk maximum, at atomic sites connecting pentagonal and hexagonal rings.

This reduction reflects the defect's inability to contribute to in-plane structural stabilization, a role inherently fulfilled by the hexagonal framework in pristine graphene. The contrasting SPTC signatures between nanotubes and graphene thus

Table 4. Summary of thermal transport signatures identified via SPTC across all materials studied in sections 4 and 5.

System	SPTC carriers	Avg. bond length [Å]	Spatial features/Nones
Amorphous Si (a-Si)	Diffusons	2.28–2.39	Filamentary high-SPTC paths; low-SPTC atoms form compact clusters.
a–c Si interface	[a] Diffusons; [c] propagons,	[a] 2.3–2.5; [c] 2.36	Gradual SPTC decline across interface; localized disorder disrupts conduction.
Silicon suboxide (SiO _x)	Localized Si-rich regions	See Ref. [80]	Hotspots in Si–Si zones; Si–O regions exhibit weak SPTC.
Fullerene (C ₆₀ -like)	Hexagons ↑; Pentagons ↓	See Ref. [81]	Reduced SPTC in pentagonal regions; curvature-dependent.
Carbon nanotube (CNT)	Uniform (pristine); defect-localized	See Ref. [82]	5–8–5 defects partially restore SPTC; vacancies suppress thermal activity.
Graphene	Uniform (pristine); defect-localized	1.42	Strong SPTC suppression at vacancy pairs (5–8–5); planar confinement enhances localization.

highlight the strong dependence of thermal activity on local lattice topology, reinforcing the interpretation of SPTC as a fundamentally local probe of thermal behavior.

5.4. SPTC Trends Across Systems

The SPTC framework reveals common transport motifs across chemically and structurally distinct systems. **Table 4** distills key characteristics of thermal transport across amorphous silicon, heterostructured interfaces, suboxides, and carbon materials, highlighting structural indicators of high and low thermal activity.

6. Conclusion

We discuss the site-projected thermal conductivity (SPTC) formalism for identifying thermally active sites in materials and begins the process of identifying thermally active defect structures in materials. We also observe that a method providing local spatial information about thermal transport opens up the possibility of studying “thermal defects” in materials, those structural irregularities that limit or destroy heat conduction.

It is not obvious that such thermal defects will be identical to electronic defects that produce localized states and/or affect electron transport. To the extent they turn out to be similar, it may be possible to properly understand the physical origin if the Wiedemann–Franz rule,^[38,88–91] at least where the phonon part of the thermal conductivity is concerned. This work hints at that because of the importance of blobs and filaments to both Urbach tails and thermal transport. It may be that a unified understanding of both thermal and electronic defects is possible. Taken together, our case studies suggest design heuristics for identifying thermally active regions in disordered and heterogeneous materials. Table 4 encapsulates these heuristics and their structural correlates across systems.

While the SPTC method offers valuable insights into microscopic heat transport, it is subject to certain limitations. First, the decomposition of the total thermal conductivity into atomic contributions—based on an analogy with Mulliken population analysis—is non-unique, reflecting some ambiguity in assigning shared quantities to individual sites. Second, the present formulation relies on the harmonic approximation, thereby neglecting anharmonic effects that may influence thermal transport, particularly at elevated temperatures. Although these effects can, in

principle, be incorporated in extended formulations, they are not captured in the current implementation.

Appendix

A. On Decay of Density Matrices

Kohn attributed the spatial locality of quantum mechanics of electrons in the solid state to destructive wave-mechanical interference between single-particle electronic states that are nearly all delocalized, even for disordered systems.^[92,93] He named this “the principle of nearsightedness.” We adopt his analysis to the thermal problem. Here, the spatial decay of Ξ , or equivalently $\rho(x - x')$ (see Equation 15), arises from the rapid decay of the FCM. In the electronic case, the density matrix ρ_e decays exponentially in insulators, and in metals, it becomes a power law decay:^[94] $\rho_e(x - x') \sim |x - x'|^{-2}$, as $|x - x'| \rightarrow \infty$. Interestingly, the decay of Ξ (or ρ) in amorphous silicon lies between these two limits: It is slower than the exponential decay characteristic of insulators but faster than the power-law decay observed in metals. This intermediate decay behavior accrues from the character of the vibrational modes in disordered systems.

B. The Spatial Decay of Force Constant Matrix

To analytically examine the behavior of SPTC, we adopted a highly simplified model using an analytical interatomic potential. Specifically, we employed the Lennard–Jones (LJ) potential to describe the interaction between two particles. The LJ potential, commonly used to capture the essential features of intermolecular forces, is given by^[53]

$$V_{LJ}(r) = \left(\left(\frac{A_m}{r} \right)^m - \left(\frac{B_n}{r} \right)^n \right) \quad (24)$$

where r is the distance between two atoms, and $n < m$. Considering the case where $n > 0$. The representation for LJ potential between two atoms, i and j , with distance, $r_{ij} = r_i - r_j$, becomes

$$U = \frac{1}{2} \sum_{i \neq j} V_{LJ}(r_{ij}) \quad (25)$$

Considering that

$$\frac{\partial}{\partial r_a^\alpha} \left(\frac{A_m}{r_{ij}} \right)^m = -\frac{m}{A_m^2} \left(\frac{A_m}{r_{ij}} \right)^{m+2} (r_i^\alpha - r_j^\alpha) (\delta_{ai} - \delta_{aj}) \quad (26)$$

the derivatives can be obtained as

$$\frac{\partial U}{\partial r_a^\alpha} = \sum_{i \neq a} \left(\frac{m}{A_m^2} \left(\frac{A_m}{r_{ia}} \right)^{m+2} (r_i^\alpha - r_a^\alpha) - \frac{n}{B_n^2} \left(\frac{B_n}{r_{ia}} \right)^{n+2} (r_i^\alpha - r_a^\alpha) \right) \quad (27)$$

For the case where $a \neq b$ (i.e., $r_{ab} \neq 0$), we have

$$\begin{aligned} \frac{\partial^2 U}{\partial r_a^\alpha \partial r_b^\beta} &= \frac{m}{A_m^4} \left(\frac{A_m}{r_{ba}} \right)^{m+4} (r_{ba}^2 \delta_{\alpha\beta} - (m+2)(r_b^\beta - r_a^\beta)(r_b^\alpha - r_a^\alpha)) \\ &\quad - \frac{n}{B_n^4} \left(\frac{B_n}{r_{ba}} \right)^{n+4} (r_{ba}^2 \delta_{\alpha\beta} - (n+2)(r_b^\beta - r_a^\beta)(r_b^\alpha - r_a^\alpha)) \end{aligned} \quad (28)$$

Considering the relationship:

$$\left| (r_b^\beta - r_a^\beta)(r_b^\alpha - r_a^\alpha) \right| < r_{ba}^2 \quad (29)$$

when $\alpha = \beta$, we have

$$\left| \frac{\partial^2 U}{\partial r_a^\alpha \partial r_b^\beta} \right| < \frac{n(n+1)}{B_n^4} \left(\frac{B_n}{r_{ba}} \right)^{n+4} r_{ba}^2 \quad (30a)$$

$$= \frac{n(n+1)}{B_n^6} \left(\frac{B_n}{r_{ba}} \right)^{n+2} \quad (30b)$$

and when $\alpha \neq \beta$, then the solution becomes

$$\left| \frac{\partial^2 U}{\partial r_a^\alpha \partial r_b^\beta} \right| < \frac{n(n+2)}{B_n^4} \left(\frac{B_n}{r_{ba}} \right)^{n+4} r_{ba}^2 \quad (31a)$$

$$= \frac{n(n+2)}{B_n^6} \left(\frac{B_n}{r_{ba}} \right)^{n+2} \quad (31b)$$

Therefore, if we consider the case where $n > 0$, then

$$\left| \frac{\partial^2 U}{\partial r_a^\alpha \partial r_b^\beta} \right| < \frac{n(n+2)}{B_n^6} \left(\frac{B_n}{r_{ba}} \right)^{n+2} \quad (32)$$

C. The Convergence of Spatial Sums for SPTC

Since both the FCM and the DM exhibit rapid spatial decay, the correlation function $\Xi(x - x')$ likewise decays for large values of $|x - x'|$. In Equation 5, the terms $e_x^{\alpha m}$, $e_{x'}^{\beta n}$, and $\frac{1}{\sqrt{m_x m_{x'}}$ are independent of system size. Therefore, to understand the system-size dependence, we must focus on the denominator terms

$$\sum_{\gamma, x, x'} \phi_{xx'}^{\alpha\beta}(0, \gamma)(\mathbf{r}) \quad (33)$$

and their spatial behavior. First we simplify the Equation 33 using the following representations

$$\mathcal{G} = \left| \phi_{xx'}^{\alpha\beta}(0, \gamma) \right| \quad (34a)$$

$$\mathbf{r} = \mathbf{R}_{xx'} + \mathbf{R}_\gamma \quad (34b)$$

$$\mathcal{G}(\mathbf{r}) = \left| \phi_{xx'}^{\alpha\beta}(0, \gamma)(\mathbf{R}_{xx'} + \mathbf{R}_\gamma) \right| \quad (34c)$$

Next, we assume the distribution of the number of pairs N from atom x to atom x' in γ th cell are uniform for large \mathbf{r} , and we represent the uniform distance as \bar{r} . The number density of pairs, ρ , relates to N as

$$dN = 4\pi r^2 \rho dr \quad (35)$$

Referencing the finite terms for atom x as \mathcal{M}_x , the size of the term in Equation 33 can be interpreted as

$$\sum_{\gamma, x, x'} \mathcal{G}(\mathbf{r}) < \sum_{\gamma, x, x'} \mathcal{G}(\mathbf{r}) \quad (36a)$$

$$\approx \sum_x \left[\mathcal{M}_x + \int_{\gamma, x'}^{(r > \bar{r})} \mathcal{G}(\mathbf{r}) dN \right] \quad (36b)$$

$$< \sum_x \left[\mathcal{M}_x + \int_{\bar{r}}^{\infty} \frac{n(n+2)}{B_n^6} \left(\frac{B_n}{r} \right)^{n+2} r 4\pi r^2 \rho dr \right] \quad (36c)$$

$$= \sum_x \left[\mathcal{M}_x + \int_{\bar{r}}^{\infty} 4\pi \rho \frac{n(n+2)}{B_n^3} \left(\frac{B_n}{r} \right)^{n-1} dr \right] \quad (36d)$$

$$= \sum_x \left[\mathcal{M}_x - \frac{n(n+2)}{(n-2)} 4\pi \rho \frac{1}{B_n^2} \left(\frac{B_n}{r} \right)^{n-2} \Big|_{\bar{r}}^{\infty} \right] \quad (36e)$$

$$= \sum_x \left[\mathcal{M}_x + \frac{n(n+2)}{(n-2)} 4\pi \rho \frac{1}{B_n^2} \left(\frac{B_n}{\bar{r}} \right)^{n-2} \right] \quad (36f)$$

Note that Equation 36f is only valid for $n > 2$. In this case, the numerator scales linearly with the number of atoms in the system (i.e., the sum over x in Equation 36f); however, this scaling is effectively canceled by the division by the system volume V in Equation 5. As a result, for $n > 2$, the expression in Equation 33 converges. Consequently, the thermal conductivity κ in Equation 5, the spatial correlation function $\Xi(x, x')$ in Equation 7, and the site-projected thermal conductivity, $\zeta(x)$, in Equation 8 are all well-defined and possess finite, convergent values.

Supporting Information

Supporting Information is available from the Wiley Online Library or from the author.

Acknowledgements

The authors thank Dr. N. Bernstein for kindly providing the amorphous-crystalline silicon interface model used in this work. The authors also gratefully acknowledge Dr. R. M. Tutchtan and Professors M. Kozicki, S. Nakhmanson, J.-J. Dong, A. Demkov, and S. R. Elliott for valuable discussions.

Conflict of Interest

The authors declare no conflict of interest.

Data Availability Statement

The data that support the findings of this study are available in the supplementary material of this article.

Keywords

dynamical matrix, heat transport, molecular simulation, site-projected thermal conductivity, thermal conductivity

Received: June 10, 2025

Revised: July 27, 2025

Published online:

- [1] P. B. Allen, J. L. Feldman, *Phys. Rev. B* **1993**, 48, 12581.
- [2] J. L. Feldman, M. D. Kluge, P. B. Allen, F. Wooten, *Phys. Rev. B* **1993**, 48, 12589.
- [3] Y. K. Koh, D. G. Cahill, *Phys. Rev. B* **2007**, 76, 075207.
- [4] F. Yang, C. Dames, *Phys. Rev. B* **2013**, 87, 035437.
- [5] D. McQuarrie, *Statistical Mechanics University Science Books*, Harper and Row, New York **1997**.
- [6] F. Müller-Plathe, *J. Chem. Phys.* **1997**, 106, 6082.
- [7] J. M. Larkin, A. J. H. McGaughey, *J. Appl. Phys.* **2013**, 114, 023507.
- [8] J. Kang, L.-W. Wang, *Phys. Rev. B* **2017**, 96, 020302.
- [9] Y. Zeng, J. T. Avritte, J. Dong, *Phys. Status Solidi B* **2021**, 258, 2000454.
- [10] Z. Zhang, Y. Guo, M. Bescond, J. Chen, M. Nomura, S. Volz, *npj Comput. Mater.* **2022**, 8, 96.
- [11] M. Simoncelli, N. Marzari, F. Mauri, *Nat. Phys.* **2019**, 15, 809.
- [12] A. Fiorentino, P. Pegolo, S. Baroni, *npj Comput. Mater.* **2023**, 9, 157.
- [13] A. Gautam, Y. G. Lee, C. Ugwumadu, K. Nepal, S. Nakhmanson, D. A. Drabold, *Phys. Status Solidi RRL* **2025**, 19, 2400306.
- [14] R. Guo, B.-Y. Cao, T. Luo, A. J. H. McGaughey, *J. Appl. Phys.* **2024**, 136, 160401.
- [15] D. R. Basaula, M. Daeipour, B. Feygelson, S. Nakhmanson, *Acta Mater.* **2024**, 271, 119889.
- [16] F. Wooten, K. Winer, D. Weaire, *Phys. Rev. Lett.* **1985**, 54, 1392.
- [17] F. H. Stillinger, T. A. Weber, *Phys. Rev. B* **1985**, 31, 5262.
- [18] E. Minamitani, T. Shiga, M. Kashiwagi, I. Obayashi, *J. Chem. Phys.* **2022**, 156, 244502.
- [19] E. Minamitani, T. Shiga, M. Kashiwagi, I. Obayashi, *J. Vac. Sci. Technol., A* **2022**, 40, 033408.
- [20] H. R. Seyf, W. Lv, A. Rohskopf, A. Henry, *Sci. Rep.* **2018**, 8, 2627.
- [21] W.-X. Zhou, Y. Cheng, K.-Q. Chen, G. Xie, T. Wang, G. Zhang, *Adv. Funct. Mater.* **2020**, 30, 1903829.
- [22] J. M. Larkin, A. J. H. McGaughey, *Phys. Rev. B* **2014**, 89, 144303.
- [23] R. Kubo, M. Yokota, S. Nakajima, *J. Phys. Soc. Jpn.* **1957**, 12, 1203.
- [24] K. N. Subedi, K. Prasai, D. A. Drabold, *Phys. Status Solidi B* **2021**, 258, 2000438.
- [25] K. Prasai, K. N. Subedi, K. Ferris, P. Biswas, D. A. Drabold, *Phys. Status Solidi RRL* **2018**, 12, 1800238.
- [26] A. Szabo, N. Ostlund, *Modern Quantum Chemistry: Introduction to Advanced Electronic Structure Theory*, Dover Books on Chemistry, McGraw-Hill, USA **1996**.
- [27] R. S. Mulliken, *J. Chem. Phys.* **1955**, 23, 1833.
- [28] P. Biswas, G. Chen, S. Nakhmanson, J. Dong, *Phys. Status Solidi B* **2021**, 258, 2100366.
- [29] A. P. Bartók, J. Kermode, N. Bernstein, G. Csányi, *Phys. Rev. X* **2018**, 8, 041048.
- [30] D. A. Greenwood, *Proc. Phys. Soc.* **1958**, 71, 585.
- [31] M. S. Green, *J. Chem. Phys.* **1954**, 22, 398.
- [32] M. Paulsson, M. Brandbyge, *Phys. Rev. B* **2007**, 76, 115117.
- [33] R. Landauer, *Philos. Mag.* **1970**, 21, 863.
- [34] B. K. Nikolić, *Phys. Rev. B* **2001**, 64, 165303.
- [35] M. Simoncelli, F. Mauri, N. Marzari, *npj Comput. Mater.* **2023**, 9, 106.
- [36] P. B. Allen, J. L. Feldman, J. Fabian, F. Wooten, *Philos. Mag. B* **1999**, 79, 1715.
- [37] P. B. Allen, J. L. Feldman, *Phys. Rev. Lett.* **1989**, 62, 645.
- [38] N. W. Ashcroft, N. D. Mermin, *Solid State Physics*, 1 ed., Holt, Rinehart and Winston, New York, USA **1976**.
- [39] L. Isaeva, G. Barbalinardo, D. Donadio, S. Baroni, *Nat. Commun.* **2019**, 10, 3853.
- [40] R. Chandra, L. Dagum, D. Kohr, R. Menon, D. Maydan, J. McDonald, *Parallel programming in OpenMP*, Morgan kaufmann, Cambridge, MA **2001**.
- [41] G. Kresse, J. Furthmüller, *Phys. Rev. B* **1996**, 54, 11169.
- [42] A. P. Thompson, H. M. Aktulga, R. Berger, D. S. Bolintineanu, W. M. Brown, P. S. Crozier, P. J. in 't Veld, A. Kohlmeyer, S. G. Moore, T. D. Nguyen, R. Shan, M. J. Stevens, J. Tranchida, C. Trott, S. J. Plimpton, *Comput. Phys. Commun.* **2022**, 271, 108171.
- [43] E. Anderson, Z. Bai, C. Bischof, S. Blackford, J. Demmel, J. Dongarra, J. Du Croz, A. Greenbaum, S. Hammarling, A. McKenney, D. Sorensen, *LAPACK Users' Guide*, 3rd ed., Society for Industrial and Applied Mathematics, Philadelphia, PA **1999**.
- [44] R. J. Hardy, *Phys. Rev.* **1963**, 132, 168.
- [45] C. Erhard, Linus, J. Rohrer, K. Albe, V. L. Deringer, *npj Comput. Mater.* **2021**, 29, 245701.
- [46] V. L. Deringer, G. Csányi, *Phys. Rev. B* **2017**, 95, 094203.
- [47] L. J. Lewis, *J. Non-Cryst. Solids* **2022**, 580, 121383.
- [48] R. A. Street, *Hydrogenated Amorphous Silicon*, Cambridge Solid State Science Series, Cambridge University Press, England **1991**.
- [49] B. R. Djordjević, M. F. Thorpe, F. Wooten, *Phys. Rev. B* **1995**, 52, 5685.
- [50] D. Igram, B. Bhattacharai, P. Biswas, D. Drabold, *J. Non-Cryst. Solids* **2018**, 492, 27.
- [51] D. M. Leitner, *Phys. Rev. B* **2001**, 64, 094201.
- [52] P. Ordejón, D. A. Drabold, R. M. Martin, S. Itoh, *Phys. Rev. Lett.* **1995**, 75, 1324.
- [53] J. E. Lennard-Jones, *Trans. Faraday Soc.* **1929**, 25, 668.
- [54] Y. F. Liu, B. Andrews, G. J. Conduit, *J. Chem. Phys.* **2019**, 150, 3.
- [55] D. A. Drabold, P. A. Fedders, O. F. Sankey, J. D. Dow, *Phys. Rev. B* **1990**, 42, 5135.
- [56] X.-P. Li, R. W. Nunes, D. Vanderbilt, *Phys. Rev. B* **1993**, 47, 10891.
- [57] M. S. Daw, *Phys. Rev. B* **1993**, 47, 10895.
- [58] X. Zhang, D. A. Drabold, *Phys. Rev. B* **2001**, 63, 233109.
- [59] K. T. Regner, D. P. Sellan, Z. Su, C. H. Amon, A. J. McGaughey, J. A. Malen, *Nat. Commun.* **2013**, 4, 1640.
- [60] J. L. Braun, C. H. Baker, A. Giri, M. Elahi, K. Artyushkova, T. E. Beechem, P. M. Norris, Z. C. Leseman, J. T. Gaskins, P. E. Hopkins, *Phys. Rev. B* **2016**, 93, 140201.
- [61] D. Surblys, H. Matsubara, G. Kikugawa, T. Ohara, *J. Appl. Phys.* **2021**, 130, 215104.
- [62] D. Surblys, H. Matsubara, G. Kikugawa, T. Ohara, *Phys. Rev. E* **2019**, 99, 051301.
- [63] S. Nosé, *Mol. Phys.* **1984**, 52, 255.
- [64] W. G. Hoover, *Phys. Rev. A* **1985**, 31, 1695.
- [65] Y. H. Lee, R. Biswas, C. M. Soukoulis, C. Z. Wang, C. T. Chan, K. M. Ho, *Phys. Rev. B* **1991**, 43, 6573.
- [66] K. Esfarjani, G. Chen, H. T. Stokes, *Phys. Rev. B* **2011**, 84, 085204.
- [67] X. Liu, X. Li, J. Liu, Z. Wang, B. Kong, X. Gong, X. Yang, W. Lin, L. Guo, *Polym. Degrad. Stab.* **2014**, 104, 62.

- [68] Y. Pan, M. Zhang, D. Drabold, *J. Non-Cryst. Solids* **2008**, 354, 3480.
- [69] F. Inam, J. P. Lewis, D. A. Drabold, *Phys. Status Solidi A* **2010**, 207, 599.
- [70] Y. Pan, F. Inam, M. Zhang, D. A. Drabold, *Phys. Rev. Lett.* **2008**, 100, 206403.
- [71] D. A. Drabold, Y. Li, B. Cai, M. Zhang, *Phys. Rev. B* **2011**, 83, 045201.
- [72] F. Urbach, *Phys. Rev.* **1953**, 92, 1324.
- [73] J. J. Ludlam, S. N. Taraskin, S. R. Elliott, D. A. Drabold, *J. Phys.: Condens. Matter* **2005**, 17, L321.
- [74] J. Dong, D. A. Drabold, *Phys. Rev. Lett.* **1998**, 80, 1928.
- [75] C. Ugwumadu, D. A. Drabold, R. M. Tutchtton, *Phys. Status Solidi B* **2025**, 2500109.
- [76] J. L. Feldman, N. Bernstein, *Phys. Rev. B* **2004**, 70, 235214.
- [77] J. a. F. Justo, M. Z. Bazant, E. Kaxiras, V. V. Bulatov, S. Yip, *Phys. Rev. B* **1998**, 58, 2539.
- [78] E. Maras, O. Trushin, A. Stukowski, T. Ala-Nissila, H. Jónsson, *Comput. Phys. Commun.* **2016**, 205, 13.
- [79] A. Stukowski, *Modell. Simul. Mater. Sci. Eng.* **2009**, 18, 015012.
- [80] C. Ugwumadu, K. Subedi, R. Thapa, P. Apsangi, S. Swain, M. Kozicki, D. Drabold, *J. Non-Cryst. Solids: X* **2023**, 18, 100179.
- [81] C. Ugwumadu, K. Nepal, R. Thapa, Y. Lee, Y. Al Majali, J. Trembly, D. Drabold, *Carbon Trends* **2023**, 10, 100239.
- [82] C. Ugwumadu, R. Thapa, Y. Al-Majali, J. Trembly, D. A. Drabold, *Phys. Status Solidi B* **2023**, 260, 2200527.
- [83] A. L. Mackay, H. Terrones, *Nature* **1991**, 352, 762.
- [84] H. Terrones, A. Mackay, *Nanostruct. Mater.* **1993**, 3, 319.
- [85] T. Lenosky, X. Gonze, M. Teter, V. Elser, *Nature* **1992**, 355, 333.
- [86] R. Thapa, C. Ugwumadu, K. Nepal, J. Trembly, D. A. Drabold, *Phys. Rev. Lett.* **2022**, 128, 236402.
- [87] C. Ugwumadu, K. Nepal, R. Thapa, D. A. Drabold, *Phys. Chem. Glasses-B* **2023**, 64, 16.
- [88] G. S. Nolas, H. J. Goldsmid, *Thermal Conductivity of Semiconductors*, Springer US, Boston, MA **2004**, pp. 105–121, ISBN 978-0-387-26017-4.
- [89] R. M. Jauhar, A. Raja, R. Rajkumar, K. Ramachandran, V. Viswanathan, K. Saravanan, P. Era, V. Malarvizhi, G. Anbalagan, M. S. Pandian, P. Ramasamy, *J. Cryst. Growth* **2022**, 578, 126427.
- [90] N. Lu, L. Li, N. Gao, M. Liu, *J. Appl. Phys.* **2016**, 120, 195108.
- [91] W. O. Wang, J. K. Ding, Y. Schattner, E. W. Huang, B. Moritz, T. P. Devereaux, *Science* **2023**, 382, 1070.
- [92] W. Kohn, A. Yaniv, *Proc. Natl. Acad. Sci.* **1978**, 75, 5270.
- [93] E. Prodan, W. Kohn, *Proc. Natl. Acad. Sci.* **2005**, 102, 11635.
- [94] G. Baym, *Lectures On Quantum Mechanics*, CRC Press, Boca Raton **2018**.

SUPPLEMENTARY MATERIAL:

Mapping Thermal Conductivity at the Atomic Scale: A Step Towards the Thermal Design of Materials

C. Ugwumadu A. Gautam Y. G. Lee D. A. Drabold

Dr. C. Ugwumadu

Quantum and Condensed Matter Physics (T-4) Group, Los Alamos National Laboratory, Los Alamos, 87545, NM, USA

A. Gautam & Prof. D. A. Drabold

Department of Physics & Astronomy, Nanoscale & Quantum Physics Institute, Ohio University, Athens, 45701, OH, USA

Y. G. Lee

Department of Physics & Astronomy, Institute of Nuclear & Particle Physics, Ohio University, Athens, 45701, OH, USA

Keywords: *thermal conductivity, molecular simulation, heat transport, SPTC, dynamical matrix*

We describe a spatial decomposition of the thermal conductivity, termed *site-projected thermal conductivity* (SPTC), which quantifies the thermal conduction activity at each atomic site—a critical parameter for the thermal design of materials. The method is based on the Green-Kubo formula and the harmonic approximation, and requires the force-constant and dynamical matrices, as well as a relaxed structural model. Throughout the paper, we use high quality models previously tested and compared to many experiments. We discuss the method and underlying approximations for amorphous silicon, carry our detailed analysis for amorphous silicon, then examine an amorphous-crystal silicon interface, and representative carbon materials. We identify the sites and local structures that reduce heat transport, and quantify these (estimate the spatial range) over which these "thermal defects" are effective. We identify filamentary structures in the amorphous silicon network which impact heat transport, and electronic structure (the Urbach edge) and electronic transport.

Sect. S1 Supporting Tables

Table S1: Cluster analysis of atoms contributing up to 75% of the total SPTC from different vibrational mode classes—propagons, diffusons, and locons—in the 512- and 4096-atom amorphous silicon (a-Si) structures. Clusters are ranked from the first (1st) to the eighth (8th) largest by size. A cluster contains at least two bonded atoms. Diffusons exhibit the longest connectivity, involving 60% of the top 25% contributing atoms in the 512-atom model and 92% in the 4096-atom model. Propagons follow with 27% connectivity in the 512-atom model, but only 2.3% in the 4096-atom model. In contrast, locons are spatially isolated, with only three atoms contributing up to 75% of the mode's maximum SPTC in both models.

512-atom Amorphous Silicon									
Modes	No. of Atoms	1 st	2 nd	3 rd	4 st	5 st	6 st	7 st	8 st
Propagons	111	31	16	5	4	3	3	2	2
Diffusons	82	49	15	4	2	2	–	–	–
Locons	3	–	–	–	–	–	–	–	–
4096-atom Amorphous Silicon									
Propagons	757	18	15	14	14	12	11	10	7
Diffusons	1187	1093	10	5	3	3	2	2	2
Locons	3	–	–	–	–	–	–	–	–

Sect. S2 Supporting Figures

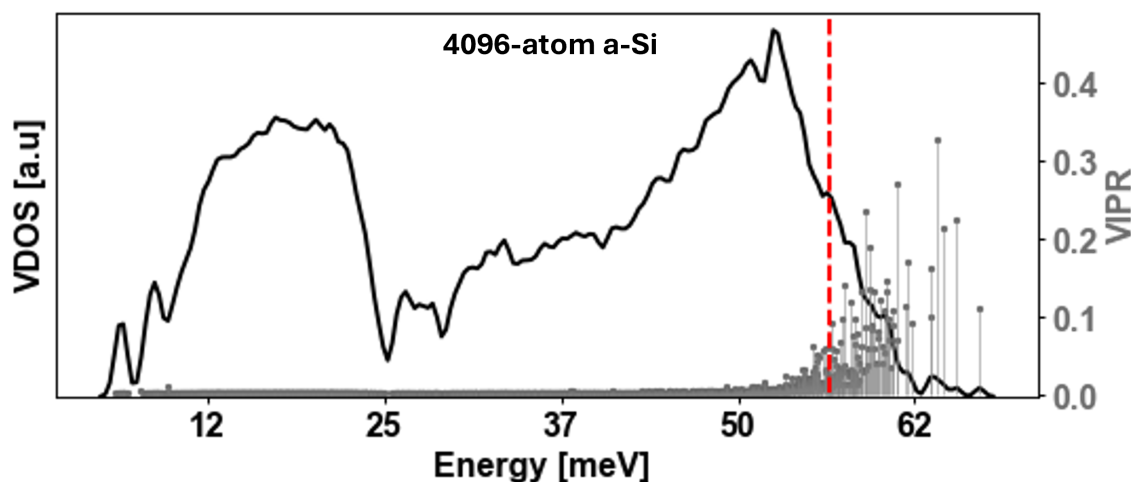


Figure S1: Vibrational density of states (VDOS, black) and vibrational inverse participation ratio (VIPR, gray) for the 4096-atom a-Si. The red dashed line at around 56.5 meV (450 cm^{-1}) denotes the approximate mobility edge, separating extended modes (propagons and diffusons) from localized modes (locons).

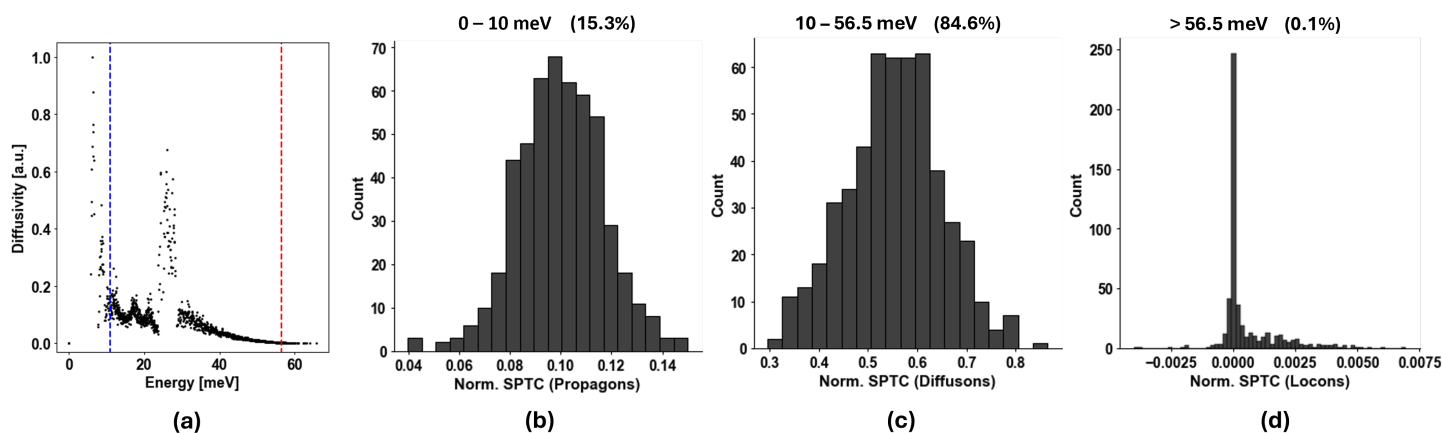


Figure S2: Vibrational mode analysis for the 512-atom a-Si model. (a) Thermal diffusivity vs. vibrational energy, with propagons (left of blue dashed line), diffusons (middle), and locons (right of red dashed line near the mobility edge). SPTC distributions from (b) propagons, (c) diffusons, and (d) locons. Insets indicate their energy ranges and percentage contributions to total SPTC. Similar plot for the 4096-atom is provided in the main text. The propagon and diffuson distributions are approximately Gaussian, with peak SPTC contributions near 10% and 55%, respectively. In contrast, the locon distribution is highly skewed, showing a narrow peak around 0.1% and a long tail.

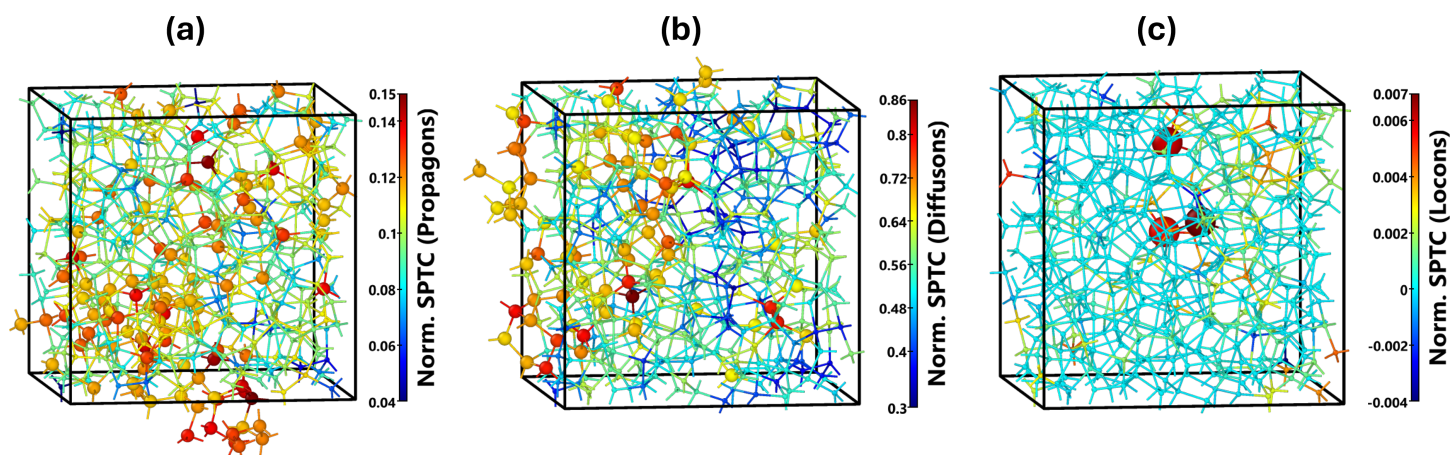


Figure S3: The contributions of (a) propagons, (b) diffusons, and (c) locons to the total SPTC are illustrated for the 512-atom model of amorphous silicon. The spatial distribution of mode-projected SPTC per atomic site is shown, with color intensity indicating the relative magnitude of each atomic site's contribution. All SPTC values are normalized by the total SPTC (i.e., without vibrational mode projection), so red regions correspond to the highest relative contributions within each mode class. Atoms contributing up to 75% of the mode's maximum SPTC (i.e., the high-SPTC range) are highlighted with increased radius. Atomic coordinates are unwrapped from periodic boundaries to better reveal the spatial connectivity of the top 75% contributors and their distribution throughout the simulation cell. The number of clustered or filamentary atoms (if any) in each mode is provided in Table S1.

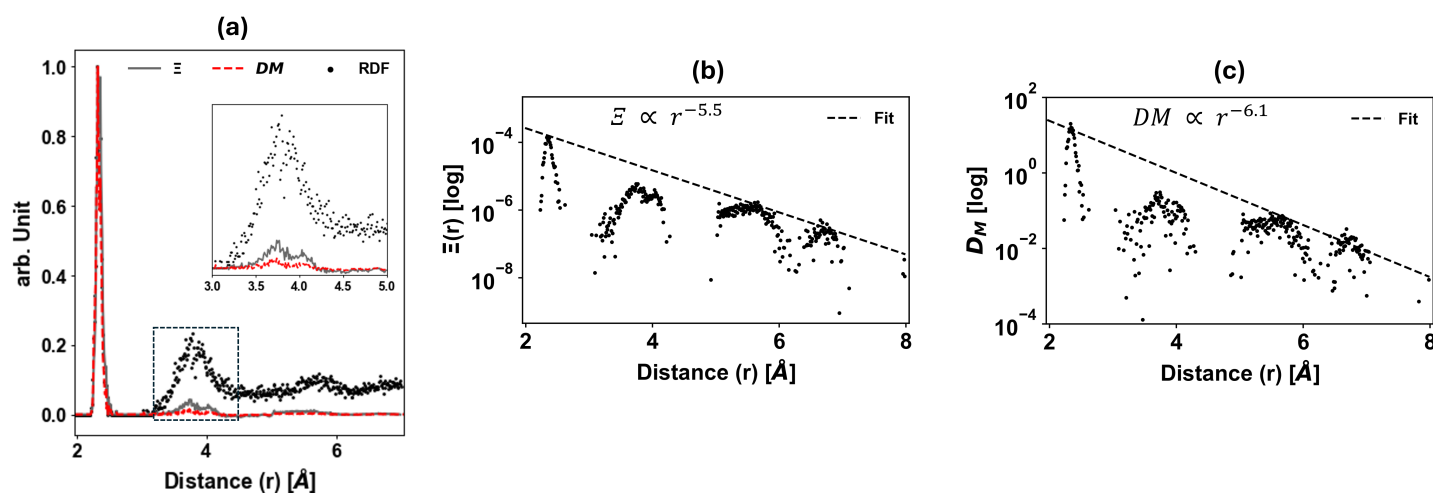


Figure S4: Spatial convergence analysis of the 512-atom amorphous silicon model. (a) Cell-averaged decay of Ξ and DM as a function of interatomic distance $r = |x - x'|$, shown alongside the radial distribution function (RDF, black) for reference. (b) Semi-logarithmic plot (log-scale on the y-axis) of Ξ illustrating exponential decay behavior, with a linear fit (dashed black line) indicating a decay rate power of 5.5. (c) Same as (b), but for DM , with a fitted decay power of 6.1. The decay rate for the 4096-atom model is 5.5 and 6.7 for Ξ and DM , respectively (see main text).

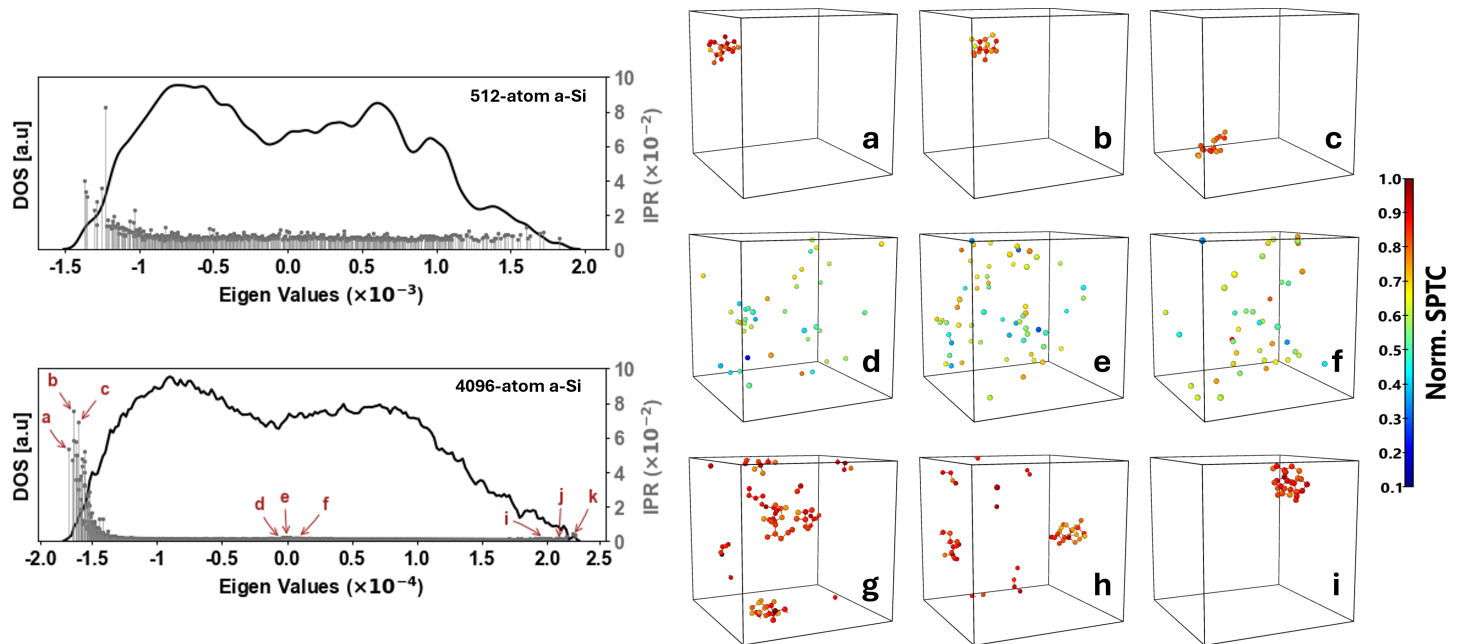


Figure S5: The density of states (DOS; black) and inverse participation ratio (IPR; gray) of the Ξ matrix, defined in Equations 7 and 15 of the main text, is shown in the top and bottom left panels for the 512- and 4096-atom amorphous silicon (a-Si) structures, respectively. Most eigenvectors of Ξ are spatially extended, except for those associated with the most negative eigenvalues (λ). For the 4096-atom system, we highlight nine representative eigenvalues (*a–i*) from three distinct regions of the spectrum, and the atoms contributing to these modes are projected in the right panels as described below: (*a, b, c*; Top) The first region, corresponding to $\lambda \ll 0$, exhibits spatially localized modes forming compact clusters (small blobs) composed of atoms with high SPTC values (see colorbar for scale). (*d, e, f*; Middle) The second region, where $\lambda \rightarrow 0$, features fully delocalized modes, as indicated by the DOS, involving atoms with low to intermediate SPTC values. (*g, h, i*; Bottom) The final region, with $\lambda \gg 0$, also includes high-SPTC atoms. However, unlike the first region, these atoms generally do not form spatially connected clusters, indicating a different localization character. A similar pattern is observed for the 512-atom a-Si structure.

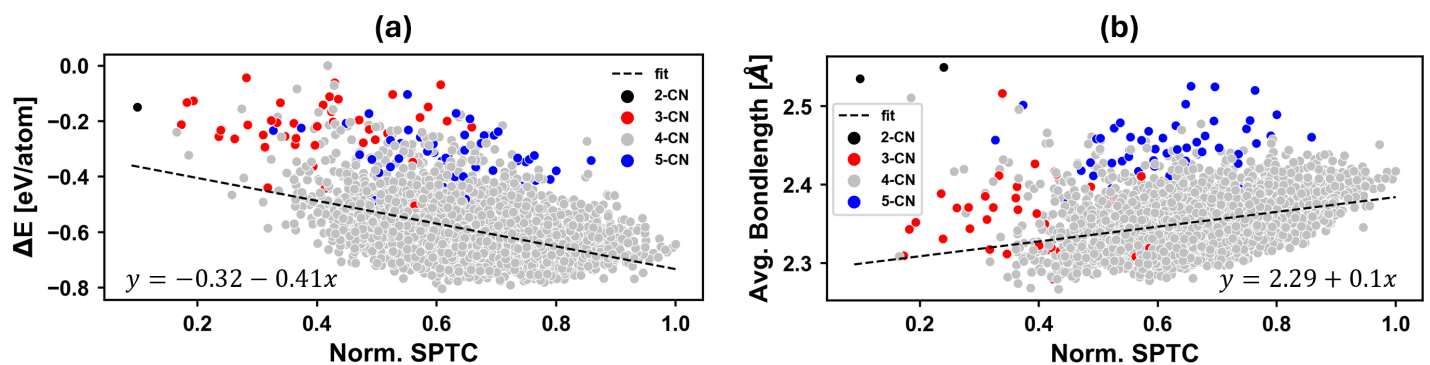


Figure S6: Thermal activity in a 4096-atom model of amorphous silicon. (a) Local atomic energy difference (ΔE) and (b) average bond length per atom plotted against Site-Projected Thermal Conductivity (SPTC), with atoms categorized by coordination number (CN). Black dashed lines indicate linear regressions; equations are provided in the insets.

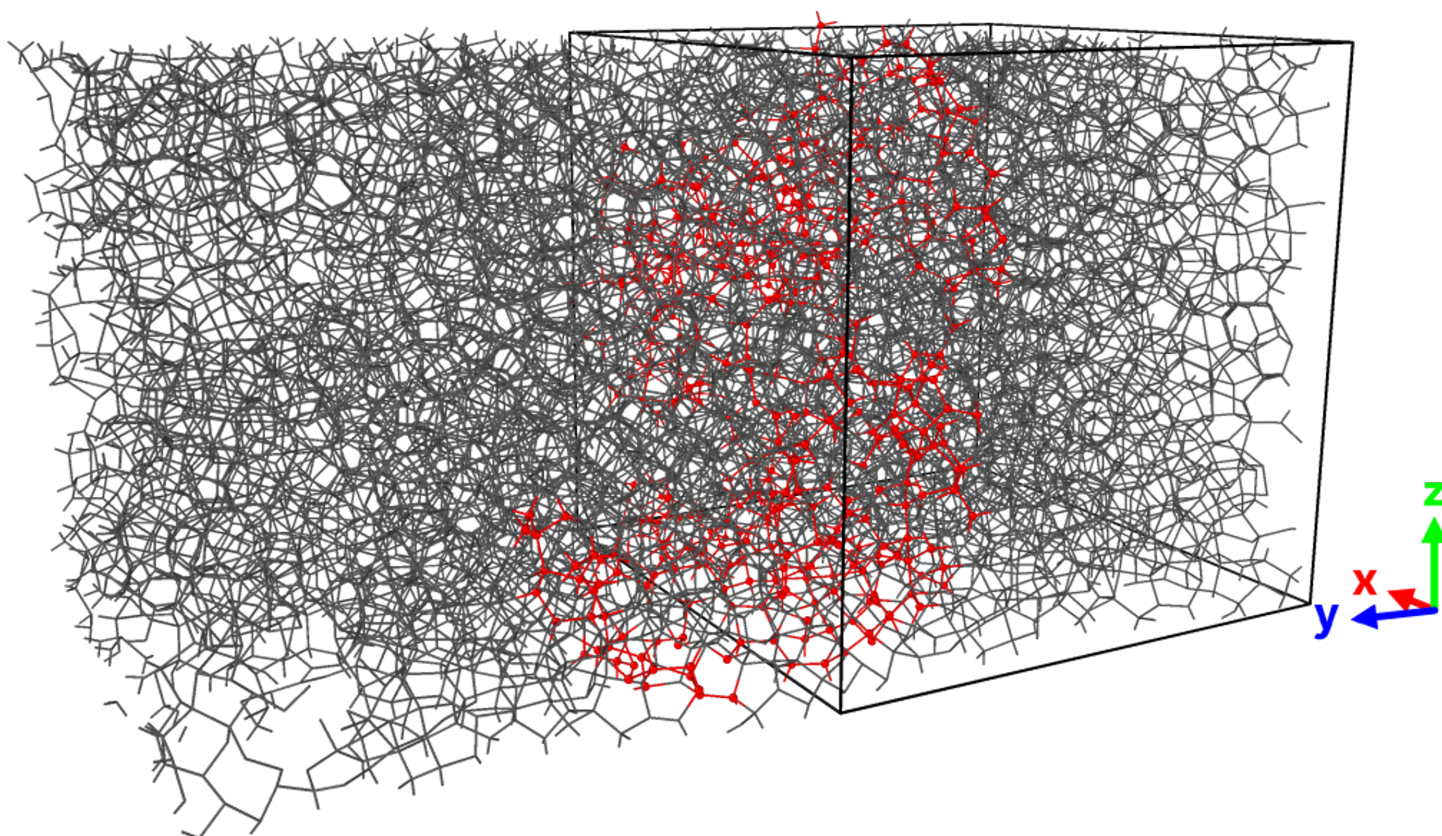


Figure S7: Heat transport network in the 4096-atom amorphous silicon model. The largest high-SPTC filament (SPTC > 75%) is shown in red, with all other atoms rendered in gray. The supercell is outlined by a black box and repeated along the y-axis to illustrate the periodic extension of the filament structure.